Determination of the absorption cross-sections of higher order iodine oxides at 355 nm and 532 nm.

Thomas R. Lewis[1,2], Juan Carlos Gómez Martín[3*], Mark A. Blitz[2], Carlos A. Cuevas[1], John M. C. Plane[2*] and Alfonso Saiz-Lopez[1*]

5   [1]Department of Atmospheric Chemistry and Climate, Institute of Physical Chemistry Rocasolano, CSIC, Madrid, Spain
[2]School of Chemistry, University of Leeds, LS29JT, Leeds, UK
[3]Instituto de Astrofísica de Andalucía, CSIC, 18008, Granada, Spain

*Correspondence to: Juan Carlos Gómez Martín (jcgomez@iaa.es), John M. C. Plane (J.M.C.Plane@leeds.ac.uk) and Alfonso Saiz-López (a.saiz@csic.es).

10   **Abstract.** Iodine oxides (I_xO_y) play an important role in the atmospheric chemistry of iodine. They are initiators of new particle formation events in the coastal and polar boundary layer and act as iodine reservoirs in tropospheric ozone-depleting chemical cycles. Despite the importance of the aforementioned processes, the photochemistry of these molecules has not been studied in detail previously. Here, we report the first determination of the absorption cross sections of I_xO_y, x = 2, 3, 5, y = 1-12 at λ = 355 nm by combining pulsed laser photolysis of I_2/O_3 gas mixtures in air with time-resolved photo-ionization time-of-flight

15   mass spectrometry, using NO_2 actinometry for signal calibration. The oxides selected for absorption cross section determinations are those presenting the strongest signals in the mass spectra, where signals containing 4 iodine atoms are absent. The method is validated by measuring the absorption cross section of IO at 355 nm, $\sigma_{355\ nm,\ IO} = (1.2 \pm 0.1) \times 10^{-18}$ cm^2, which is found to be in good agreement with the most recent literature. The results obtained are: $\sigma_{355\ nm,\ I2O3} < 5 \times 10^{-19}$ cm^2 molecule^{-1}, $\sigma_{355\ nm,\ I2O4} = (3.9 \pm 1.2) \times 10^{-18}$ cm^2 molecule^{-1}, $\sigma_{355\ nm,\ I3O6} = (6.1 \pm 1.6) \times 10^{-18}$ cm^2 molecule^{-1}, $\sigma_{355\ nm,\ I3O7} = (5.3$

20   $\pm 1.4) \times 10^{-18}$ cm^2 molecule^{-1} and , $\sigma_{355\ nm,\ I5O12} = (9.8 \pm 1.0) \times 10^{-18}$ cm^2 molecule^{-1}. Photodepletion at λ = 532 nm was only observed for OIO, which enabled determining upper limits for the absorption cross sections of I_xO_y at 532 nm using OIO as an actinometer. These measurements are supplemented with ab-initio calculations of electronic spectra in order to estimate atmospheric photolysis rates $J(I_xO_y)$. Our results confirm a high $J(I_xO_y)$ scenario where I_xO_y is efficiently removed during daytime, implying enhanced iodine-driven ozone depletion and hindering iodine particle formation. Possible I_2O_3 and I_2O_4

25   photolysis products are discussed, including IO_3, which may be a precursor to iodic acid (HIO_3) in the presence of HO_2.

1. Introduction

Photolabile iodine-containing molecules are emitted into the lower atmosphere from the sea surface and from marine biota. The atmospheric processing of iodine leads to its accumulation in aerosol, subsequent transport and deposition on land, where it enters the continental ecosystems (Saiz-Lopez et al., 2012b). In the course of this process, gas-phase reactive iodine is

30   involved in two important chemical processes of the background troposphere: ozone depletion and new particle formation .
Iodine is thought to be responsible for 9 to 16% of the contemporary ozone removal in the tropical troposphere (Saiz-Lopez et
al., 2014), and there is evidence that anthropogenic ozone pollution enhances iodine release from the sea surface (Carpenter et
al., 2013; Chance et al., 2014; MacDonald et al., 2014; Prados-Roman et al., 2015; Cuevas et al., 2018), which in turn has
accelerated ozone loss in the last decades (Cuevas et al., 2018). The atmospheric chemistry of iodine is in principle fairly

35   simple, since the main atmospheric fate of the iodine atoms is reaction with ozone to form iodine monoxide (IO). This radical
photolyzes readily (Gómez Martín et al., 2005), creating an ozone-neutral cycle and establishing a steady state concentration
of I and IO, which are then termed collectively as active iodine or IO_x. Any other chemical cycle involving IO which recycles
atomic iodine without concomitant generation of atomic oxygen leads to ozone depletion, e.g. (Gómez Martín et al., 2009):

$$I + O_3 \rightarrow IO + O_2 \tag{R1}$$

40   $$IO + IO \rightarrow OIO + I \tag{R2}$$

$$OIO + h\nu \rightarrow I + O_2 \tag{R3}$$

Net: $2O_3 \rightarrow 3O_2$
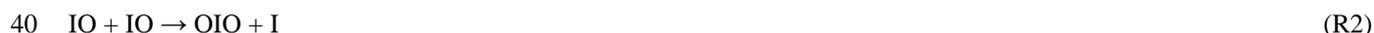
Further steps in this scheme lead to the formation of higher iodine oxides (Gómez Martín et al., 2013):

$$IO + IO \rightarrow I_2O_2 \tag{R4}$$

45   $$IO + OIO \rightarrow I_2O_3 \tag{R5}$$

$$OIO + OIO \rightarrow I_2O_4 \tag{R6}$$

$$I_xO_y + I_xO_y \rightarrow\rightarrow\rightarrow \text{ particles} \tag{R7}$$

Previous laboratory experiments on iodine photochemistry have reported kinetic growth of broad band absorptions following
the decay of IO and OIO as well as significant deposition of particulates on the walls of the reactors (Cox and Coker, 1983;

50   Laszlo et al., 1995; Harwood et al., 1997; Gómez Martín et al., 2005). These broad band absorbers have been tentatively
identified as some of the higher iodine oxides produced in reactions R4, R5 and R6 (Bloss et al., 2001; Gómez Martín et al.,
2007), which are believed to be precursors to the particles that eventually deposit on the walls. Furthermore, iodine oxide
containing particles have been observed in multiple aerosol flow tube and steady state chamber experiments starting from the
photooxidation of iodine precursors directly injected into the chamber (Hoffmann et al., 2001; Jimenez et al., 2003; Saunders

55   et al., 2010; Wei et al., 2017) or emitted from cultures of algae under oxidative stress (McFiggans et al., 2004; Pirjola et al.,
2005). Emissions of I_2 and alkyl-iodides from coastal macroalgae and polar phytoplankton and concurrent observation of IO
and OIO (Saiz-Lopez and Plane, 2004) have been unambiguously linked to intense new particle formation events (Jimenez et
al., 2003; McFiggans et al., 2004). Thus, there is a strong indication that iodine oxide clustering also happens in the coastal
boundary layer and is responsible for particle formation events.

60 Recent Chemical Ionization - Atmospheric Pressure Interface- Time of Flight Mass Spectrometry (CI-API-ToF-MS) observations of IO_3^- and IO_3-containing ion clusters in coastal and polar environments, as well as complementary laboratory experiments in the absence of HO_x, have been interpreted as direct measurements of gas-phase iodic acid ($HOIO_2$, hereafter denoted as HIO_3) and HIO_3 clusters (Sipilä et al., 2016). Since all possible reaction paths between H_2O and I, IO and OIO are very endothermic (Canneaux et al., 2010; Hammaecher et al., 2011; Khanniche et al., 2017a), and IO_x–H_2O complexes are

65 very weakly bound (Galvez et al., 2013), the formation of oxyacids may rather proceed via hydrolysis of higher iodine oxides (Kumar et al., 2018):

$$I_2O_y + H_2O \rightarrow HIO_x + HIO_{y-x+1} \tag{R8}$$

Ozone depletion and particle formation are to some extent competing processes. Significant I_xO_y photolysis rates may result in regeneration of IO_x:

70 $$I_2O_2 + h\nu \rightarrow IO + IO \tag{R9a}$$

$$\rightarrow I + OIO \tag{R9b}$$

$$I_2O_3 + h\nu \rightarrow IO + OIO \tag{R10a}$$

$$\rightarrow I + IO_3 \tag{R10b}$$

$$I_2O_4 + h\nu \rightarrow OIO + OIO \tag{R11a}$$

75 $$\rightarrow IO + IO_3 \tag{R11b}$$

These photochemical reactions would enhance ozone depletion, while slowing down the incorporation of iodine into aerosol via oxides and/or oxyacids. This is currently an important uncertainty in the iodine chemical mechanism incorporated into global chemistry transport models (Saiz-Lopez et al., 2014; Sherwen et al., 2016). In order to reduce this uncertainty, we report here a set of I_xO_y photodepletion experiments with mass spectrometric detection, which enables unambiguous observation of

80 all the species of interest (Gómez Martín et al., 2013). Experiments devoted to understanding the interaction between I_xO_y and water, potentially leading to the formation of HIO_3, will be reported elsewhere.

2. Methods

2.1. Experimental set-up

A pulsed laser photolysis (PLP) system has been employed to generate iodine oxides from the photolysis of O_3 in the presence

85 of I_2 in a tubular reaction cell (Figure 1). A flow of typically 1.5 slm of He carrier gas (99.999%, BOC Gases) was introduced in the reactor. I_2 molecules were entrained in the carrier flow by passing a smaller flow of He (~100 sccm) through a 12 mm diameter temperature-stabilized Teflon tube containing I_2 crystals (>99.5%, Sigma-Aldrich). An electrical discharge ozone

generator converted ~2% of a ~100 sccm O_2 flow (99.999%, BOC Gases) to O_3, which was introduced to the main flow via an inlet on the flow tube.
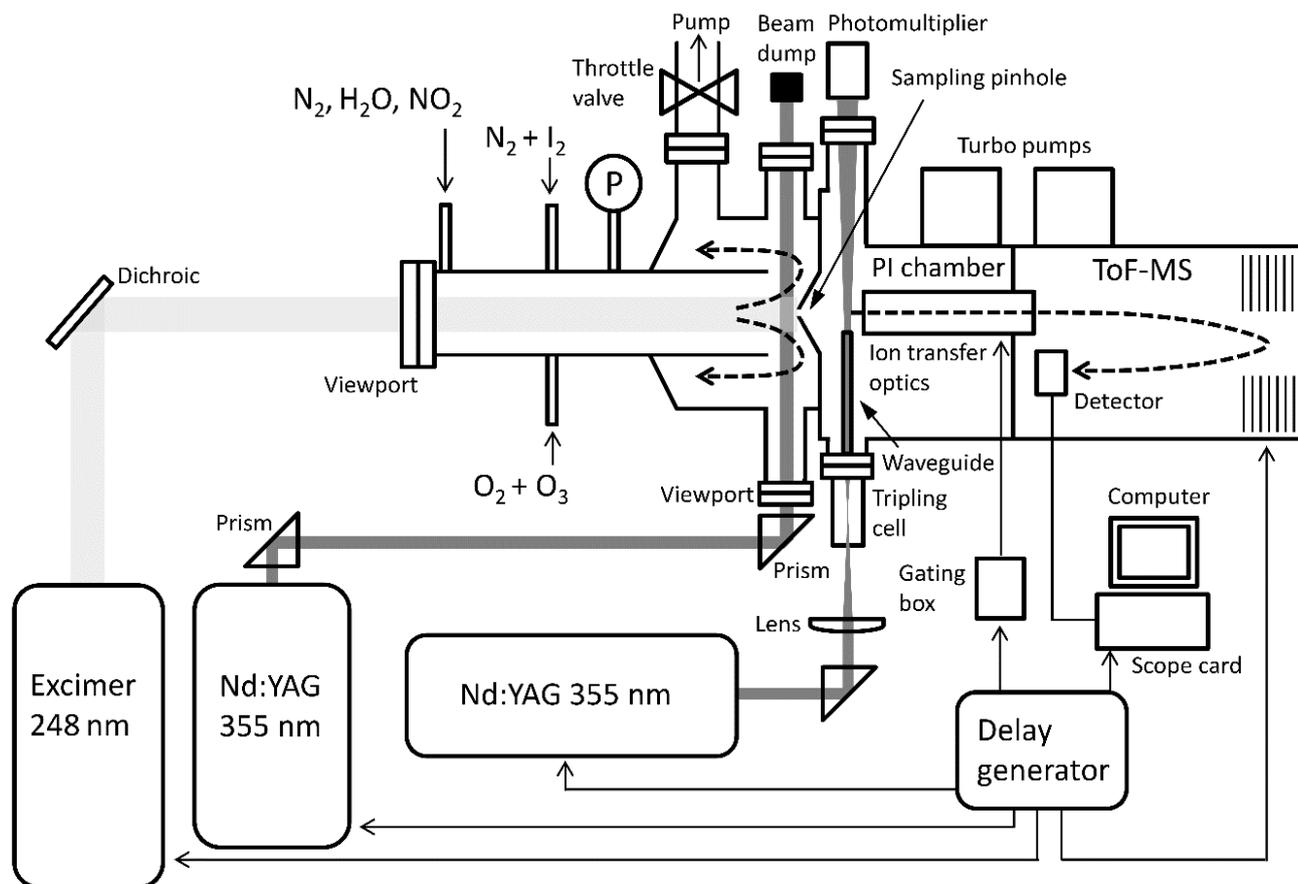
Figure 1: Schematic diagram of the experimental set-up for studying the photolysis of iodine oxides

90   Ozone was photolyzed at 248 nm by an excimer laser beam (Lambda Physik Compex 102), which was passed unfocussed through a quartz viewport along the tube main axis. This generated the well-known sequence of reactions:

$$O_3 + hv \rightarrow O(^1D) + O_2 \tag{R12}$$

$$O(^1D) + M \rightarrow O(^3P) + M \tag{R13}$$

$$O(^3P) + I_2 \rightarrow IO + I \tag{R14}$$

95   followed by reactions R1, R2, R4, R5 and (R6), as well as further I_xO_y clustering reactions. The precursor concentrations ($[I_2]$~ 4×10^{14} molecule cm^{-3}, $[O_3]$~ 5×10^{14} molecule cm^{-3}) and laser energy (120 mJ pulse^{-1}) were tuned to ensure that I_2 was in excess over $O(^3P)$. Iodine and ozone concentrations were measured using a 532 nm solid state laser in a single pass and a multipass Herriot cell (Lewis et al., 2018), respectively (Figure 2). A reflection (~5%) of the main 532 nm diode laser (Thorlabs

CPS532 532 nm 4.5 mW) beam was directed along the length of the cell (length = 40 cm) and detected using a photodiode
100 detector (Thorlabs SM05PD3A). Ozone was detected by passing the main beam through a hole in the rear of a silver-coated
concave mirror (Thorlabs CM508-200-P01 f = 20 cm) onto an identical mirror (without a hole) positioned 40 cm from the first
mirror. The light was passed 40 times through the cell, and exits through the same entrance hole (some passes are omitted from
the diagram for simplicity), giving a path length of 12 m.`
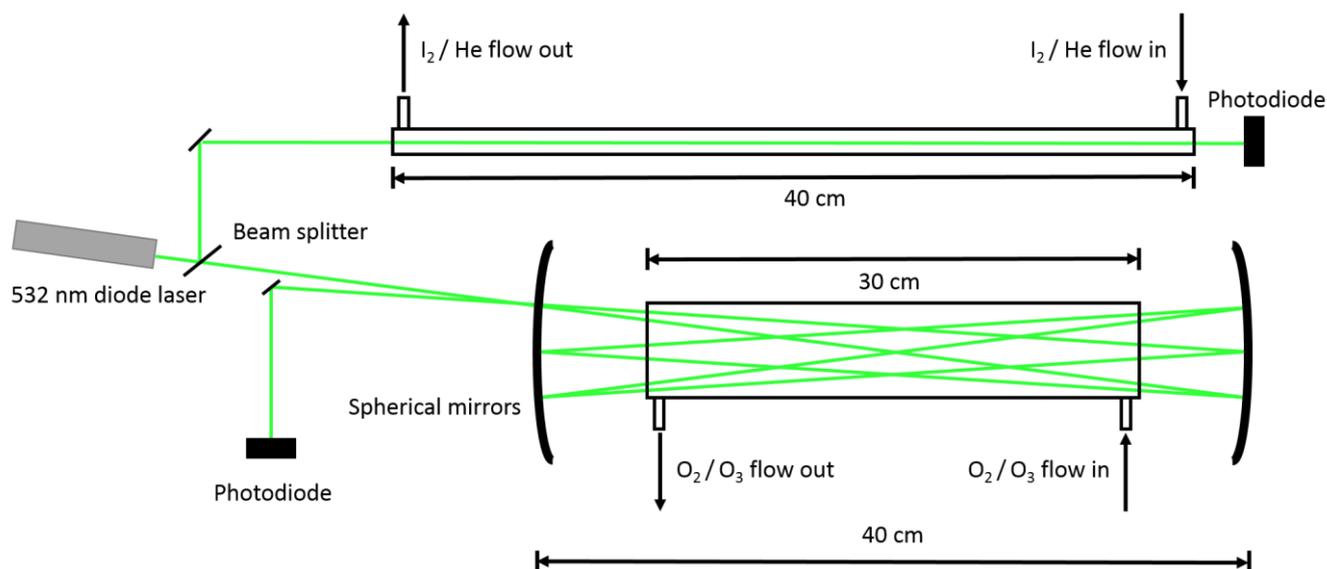
Figure 2: A Schematic of the absorption setup used to measure both I₂ and O₃

The concentrations C of O_3 and I_2 were then determined using the Beer-Lambert law (equation 1), where I and I_0 are the
105 intensities of the 532 nm laser light recorded with and without the reagent present, respectively, OD is the optical density, σ
the absorption cross section, and l the optical path length:

$$OD = \ln\frac{I_0}{I} = \sigma \cdot C \cdot l \tag{1}$$

O_3 has an absorption cross-section at 532 nm of 2.34×10^{-21} cm² molecule⁻¹ (Burrows et al., 1999). A typical concentration of
5×10^{14} molecule cm⁻³ in the reaction mixture (total flow ~1700 sccm) requires a concentration in the O_3/O_2 flow (100 sccm)
110 of around 8.5×10^{15} molecule cm⁻³. An ozone concentration of 8.5×10^{15} molecule cm⁻³ results in OD = 0.024. I_2 has an
absorption cross-section at 532 nm of 3.03×10^{-18} cm² molecule⁻¹(Saiz-Lopez et al., 2004). A typical I_2 concentration of 4 ×
10^{14} molecule cm⁻³ in the reaction mixture (total flow ~1700 sccm) requires a concentration in the I_2/He flow (100 sccm) of
around 6.8×10^{15} molecule cm⁻³. An I_2 concentration of 6.8×10^{15} molecule cm⁻³, giving OD = 0.62. The ODs observed for
both species are easily detectable by the instrument, which has a typical signal-to-noise ratio of ~ 400.
115 In order to measure the photodepletion of the I_xO_y molecules at 532 nm and 355 nm, a frequency-doubled or tripled Nd:YAG
laser beam (Continuum Surelite 10-II, 1 cm⁻¹ linewidth, 20 ns pulse width, ~80 mJ pulse⁻¹ at 532 nm and ~50 mJ pulse⁻¹ at
355 nm) was passed across the flow tube, perpendicular to the main axis and near the sampling point. Experiments were carried

out at 4-7 Torr. The pressure in the reactor was set by a throttle valve placed upstream of an Edwards 80 roots blower – oil

rotary pump combination. The flows were set using MKS calibrated mass flow controllers and pressure was measured using a

120   set of 10 Torr and 1000 Torr MKS Baratron pressure transducers.
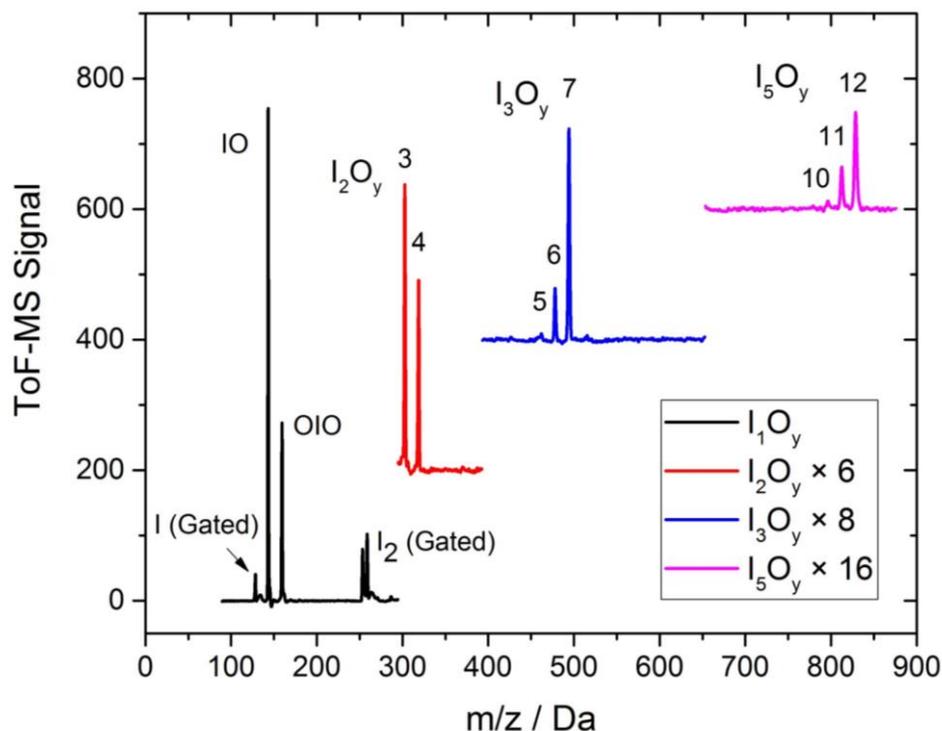
Figure 3: Mass spectra in four different m/z ranges encompassing peaks of species with 1, 2, 3 and 5 iodine atoms. Some of the spectra are scaled and shifted for clarity.

The iodine oxides generated were sampled in situ from the irradiated volume through a pinhole (200 μm diameter) situated on

axis into a Kore Technology photo-ionization time-of-flight mass spectrometer (PI-ToF-MS) described in detail elsewhere

(Gómez Martín et al., 2016). The PI chamber of this instrument (~10^{-4} Torr) is fitted with viewports, allowing a pulsed laser

beam to be directed through the high density region of the sampled gas jet. Iodine oxides have ionization potentials in the

125   range of 9-11 eV (Gómez Martín et al., 2013; Wei et al., 2017), which requires generating a vacuum ultraviolet (VUV) laser

ionization beam. This is achieved by tightly focusing the 355 nm output of a frequency-tripled Nd:YAG laser (Continuum

Surelite 10-II) in a cell filled with xenon, which produces VUV radiation by frequency tripling (118 nm , or equivalently 10.5

eV) (Kung et al., 1973; Mahon et al., 1979). The resulting positive ions are accelerated towards the ToF-MS by means of a

continuous negative voltage. An electron photomultiplier detector coupled to a pre-amplifier outputs an analog signal, which

130   is registered by the digital oscilloscope (Picoscope 6000). A limitation of this method is that large signals (e.g. I_2^+ and I^+) cause

detector overload during a significant time span after the large peak has been registered. An analog gating box is used to lessen

these effects by sending a (~ 400 ns wide) gating pulse to the ion extraction optics. Gating in this way removed >90% of the

overloaded signal from I_2^+ and I^+, significantly improving the signal to overload ratio.

Synchronization between the chemistry-initiating laser pulse, the photolysis laser, the probing PI laser pulse and the detection

135   devices is provided by a computer-controlled delay generator (Quantum Composers, 9518). In this manner, the delay between

PLP and PI can be varied in order to observe the kinetics of reactants and products, and the photodepletion of the species of

interest. The experiment repetition rate was set at 10 Hz, the optimal repetition rate for operation of both the VUV generating

PI YAG laser and the YAG laser used for photolysis of the iodine oxides. A LabView program built in-house provides a

sequence of delays between the PLP and PI lasers which can be modified by the user via a graphical interface. Desired

140   experimental parameters are input into the LabView program, including the number of pre-photolysis points, the number of

experimental data, the duration of the experiment and the number of repetitions. Each experiment results in a 3-dimensional

dataset of signal intensity (proportional to concentration) vs. photolysis-photoionization delay and time-of-flight (Figure 3).

Mass-to-charge (m/z) calibration of time-of-flight was performed by selecting a number of well-known prominent mass peaks

(e.g. IO at m/z =143, OIO at m/z =159, I_2O_3 at m/z =302, I_2O_4 at m/z =318 and I_3O_7 at m/z =493 (Gómez Martín et al., 2013)).
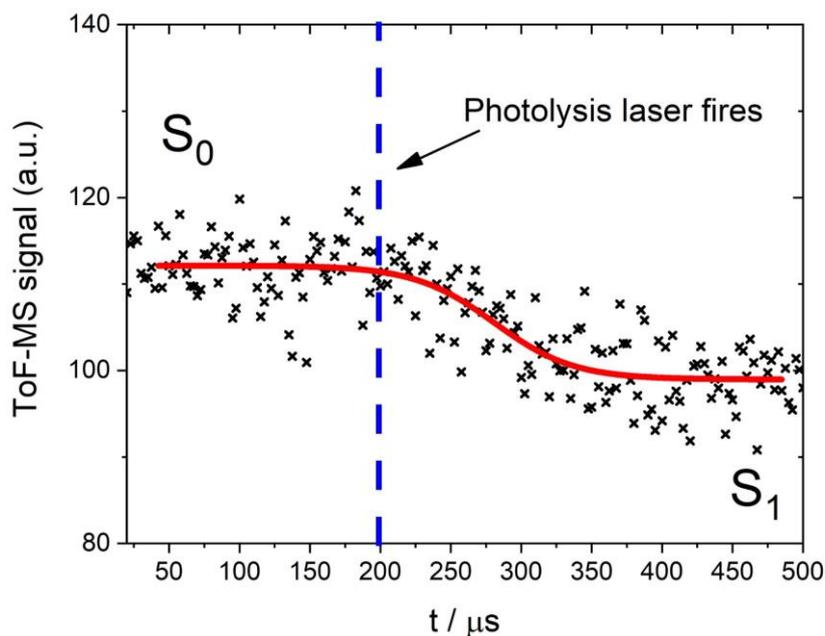
Figure 4: Schematic of a photodepletion measurement of NO_2. The red curve is an empirical fit through the data performed to obtain the values of S_0 and S_1.

145   To investigate the photodepletion of I_xO_y, it is desirable to keep the signal of the species of interest relatively constant over the

delay window used to probe the photolysis. The timing of the Nd:YAG photolysis laser shot was programmed to a fixed delay

with respect to the 248 nm excimer flash. To find the optimal window in which to conduct photolysis experiments, the reaction

kinetics were first explored between 0 and ~10 ms for different sets of conditions. It was important to generate a sufficiently

high concentration of I_xO_y to obtain a good signal-to-noise ratio, but not so high that the growth/removal timescale was

150   comparable to the observed photodepletion (~400 μs). Fragmentation of iodine oxides was a significant problem in these

experiments where the amount of active iodine (IO_x = I, IO) released from reaction R12 is high, leading to fast formation of

I_xO_y and particles. Under these conditions, at long times after the peak IO and OIO (~3-5 ms), the observed signal of IO, OIO and I_xO_y is contaminated by photofragmentation of higher order iodine oxides. For this reason, great care needed to be taken to establish a time window for each species wherein higher oxides are not present, to ensure that any depletion in the mass

155 spectrometric signal for each species is exclusively due to the removal of the species via photolysis. Evidence of fragmentation comes in the form of a secondary growth in the signal seen for IO and OIO. The delay between the excimer and the Nd:YAG photolysis laser was therefore carefully selected to coincide with a period of relatively constant signal of the desired analyte, typically a maximum for short lived species, or a slow rise for larger reaction products of interest.

The photolysis laser depletes any analyte within the photolysis volume which exhibits a bound-unbound transition at the energy

160 of the photolysis wavelength used for each experiment. The signals for a certain m/z ratio before and after the photolysis laser is fired are respectively noted as S_0 and S_1 (Figure 4). Absorption cross sections were then calculated by comparing the relative signal change (ζ_{IxOy}) for the analyte of interest to the relative signal change (ζ_{REF}) for a molecule having a well-studied spectrum in an analogous actinometric experiment using the same configuration and laser fluence. In this way, systematic errors arising from the beam energy and area are eliminated in the determination of the actinic flux F:

165
$$\frac{S_{REF\,0}-S_{REF}}{S_{REF\,0}} = \frac{[X_{REF}]_0-[X_{REF}]}{[X_{REF}]_0} \equiv \zeta_{REF} = 1 - e^{-F \cdot \sigma_{X_{REF}} \cdot \phi_{X_{REF}}} \tag{2}$$

$$F = -\frac{1}{\sigma_{X_{REF}} \cdot \phi_{X_{REF}}} \ln(1-\zeta_{REF}) \tag{3}$$

Similarly, for the target I_xO_y molecule we have:

$$\frac{S_{IxOy\,0}-S_{IxOy}}{S_{IxOy\,0}} = \frac{[I_xO_y]_0-[I_xO_y]}{[I_xO_y]_0} \equiv \zeta_{I_xO_y} = 1 - e^{-F \cdot \sigma_{I_xO_y} \cdot \phi_{I_xO_y}} \tag{4}$$

$$\sigma_{I_xO_y} \cdot \phi_{I_xO_y} = -\frac{1}{F}\ln(1-\zeta_{I_xO_y}) \tag{5}$$

170 Inserting equation 3 in equation 5, we have:

$$\sigma_{I_xO_y} \cdot \phi_{I_xO_y} = \sigma_{X_{REF}}\phi_{X_{REF}} \frac{\ln(1-\zeta_{I_xO_y})}{\ln(1-\zeta_{REF})} \tag{6}$$

NO_2 (99.5%, BDH, 10% in He) was the best reference molecule to perform actinometry at 355 nm. In this case, $\sigma_{X_{REF}} = \sigma_{NO_2(355\,nm)} = 5.3 \times 10^{-19}$ cm^2 molecule^{-1} (Vandaele et al., 1998) and $\phi_{X_{REF}} = \phi_{NO_2(355\,nm)} = 1$ (Burkholder et al., 2015). Typically, NO_2 depletion was around 8% in the actinometric experiments. For the 532 nm photolysis experiments, OIO was

175 chosen as reference, owing to the low sensitivity of its broad absorption bands to photolysis laser resolution (as opposed, for example, to I_2) and relatively well known absorption cross sections (Bloss et al., 2001; Gómez Martín et al., 2005). Thus $\sigma_{X_{REF}} = \sigma_{OIO(532\,nm)} = 9.5 \times 10^{-18}$ cm^2 molecule^{-1} and $\phi_{X_{REF}} = \phi_{OIO(532\,nm)} = 1$ (Gómez Martín et al., 2009). In principle, equation 6 yields the photolysis cross section, i.e. the product $\sigma_{I_xO_y} \cdot \phi_{I_xO_y}$, which is equal to the absorption cross section if $\phi_{I_xO_y} = 1$. This is a reasonable assumption for broad band absorption spectra.

180 **2.2. Ab initio calculations**

The geometry of the ground electronic state of IO_3, I_2O_3, I_2O_4, I_3O_6 and I_3O_7 was optimized by using the B3LYP functional combined with the standard 6-311+G(2d,p) triple-ζ basis set for O and H, and an all-electron (AE) basis set for I (Glukhovtsev et al., 1995). The AE basis set is a contracted (15s12p6d)/[10s9p4d] 6-311G basis, the [5211111111,411111111,3111] contraction scheme supplemented by diffuse s and p functions, together with d and f polarization functions. See Glukhovtsev

185 et al. (1995) for further details. Figure 5 illustrates the geometries of the various iodine oxides and hydroxy- species that are discussed in Section 4. The corresponding molecular parameters (Cartesian coordinates, rotational constants and vibrational frequencies) are listed in **Table *1***.

Table 1: Molecular properties of I_2O_3, I_2O_4, I_3O_6 (cyclic), I_3O_6 (linear), I_3O_7 (cyclic), I_3O_7 (linear), IO_3 and the transition state for dissociation of IO_3 to $IO + O_2$ (illustrated in Figure 5); and the stationary points on the $IO_3 + HO_2$ surface (Figure 11).

Molecule	Cartesian co-ordinates /Å [a]	Rotational constants /GHz [a]	Vibrational frequencies /cm^{-1} [a]
I_2O_3	I, -0.009, -0.201, -0.192 O, -1.208, -0.160, 1.377 I, -0.583, 0.643, 3.128 O, 0.427, 1.521, -0.391 O, 1.423, -1.065, 0.438	4.46970, 0.57042, 0.55739	44, 88, 241, 256, 299, 450, 624, 872, 902
I_2O_4	O, -1.655, -0.203, 1.563 I, 0.046, 0.313, 1.770 O, 0.699, 0.048, -0.103 O, 0.936, -0.982, 2.619 I, -0.385, -0.913, -1.502 O, -1.272, 0.428, -2.370	3.55600, 0.49098, 0.47135	48, 67, 92, 164, 248, 260, 308, 444, 538, 812, 874, 906
I_3O_6 (cyclic)	I, 1.335, -1.791, -0.031 O, 1.569, 0.091, -0.823 O, 3.064, -2.228, 0.378 I, 1.319, 1.750 , 0.186 O, -0.279, 1.411, 0.952 O, 1.051, 2.850, -1.192 I, -2.620, -0.026, 0.066 O, -1.412, -1.310, -0.437 O, -4.280, -0.729, -0.202	0.44642, 0.26455, 0.17279	18, 26, 54,59, 66, 70, 87, 107, 116, 171, 202, 274, 295, 319, 444, 563, 783, 804, 814, 843, 898
I_3O_6 (linear)	O, -0.860, 0.445, 0.841 I, -0.142, -0.977, -0.191 O, 1.698, -0.828, 0.694 O, -2.369, -1.079, -0.706 I, 3.054, 0.513, 0.198 O, 2.321, 1.165, -1.301 O, 4.415, -0.561, -0.236 I, -3.219, 0.313, 0.228 O, -3.185, 1.803, -0.797	1.40546, 0.15363, 0.14491	21, 33, 60, 69, 85, 98, 122, 166, 184, 262, 268, 302, 313, 343, 442, 565, 664, 699, 843, 871, 903
I_3O_7 (cyclic)	I, 1.050, -1.602, -0.490 O, 1.254, 1.127, -0.500	0.43718, 0.25525, 0.17036	29, 49, 61, 66, 79, 82, 90,

	O, 1.159, -3.334, -0.902 I, 0.374, 2.634, 0.070 O, -1.810, 0.925, 0.501 O, 1.558, 4.011, -0.093 I, -2.237, -0.789, 0.151 O, 0.594, -1.505, 1.245 O, -3.595, -0.762, -1.001 O, -0.813, -1.235, -1.152		111, 123, 171, 186, 262, 279, 302, 308, 324, 494, 566, 782, 807, 852, 862, 905, 909
I_3O_7 (linear)	O, 4.334, 1.318, 0.098 I, 3.552, -0.283, 0.217 O, 1.828, 0.194, 0.994 O, 2.970, -0.766, -1.411 I, 0.004, 0.013, 0.002 O, -1.823, -0.085, -0.997 O, 0.008, -1.794, 0.247 I, -3.543, -0.351, -0.118 O, -2.958, -0.382, 1.579 O, -4.337, 1.219, -0.426	2.11361, 0.11760, 0.11718	21, 25, 33, 44, 46, 60, 84, 140, 186, 203, 263, 266, 296, 312, 320, 418, 433, 552, 635, 759, 867, 867, 901, 902
IO_3	I, 0.080, 1.235, 0.000 O, 0.645, -0.481, 0.000 O, 0.645, 2.092, 1.486 O, 0.645, 2.092, -1.486	6.18204, 6.18204, 3.57497	258, 258, 268, 766, 766, 799
TS for $IO_3 \rightarrow IO + O_2$	I, 0.205, 0.253, -0.082 O, 1.400, -1.046, 0.249 O, -1.406, -0.589, -0.790 O, -1.419, -0.181, 0.909	8.93231, 4.04781, 3.81028	-914, 142, 252, 354, 701, 867
IO_3-HO_2 complex	I, -0.649, 0.251, 0.072 O, -0.420, -1.455, 0.587 O, -0.429, 1.299, 1.501 O, 1.098, 0.455, -0.961 O, 2.104, -0.347, -0.326 O, 2.090, -1.626, -0.927 H, 1.449, -2.095, -0.357	4.44296, 1.49686, 1.34348	64, 143, 192, 226, 297, 316, 464, 530, 568, 719, 860, 903, 938, 1453, 3638
TS from IO_3-complex to HIO_3 + O_2	I, 0.131, 1.178, -0.047 O, 0.550, -0.594, 0.341 O, 0.383, 2.058, 1.482 O, 1.579, 1.575, -1.172 O, 2.931, 0.475, -0.440 O, 2.661, -0.726, -0.774 H, 1.671, -0.878, -0.163	4.24271, 1.59293, 1.46409	1000i, 74, 225, 250, 288, 323, 377, 500, 624, 711, 823, 904, 1246, 1306, 1749
HIO_3	I, 1.574, -0.480, 0.151 O, -0.137, -0.710, -0.315 O, 2.309, 0.401, -1.439 O, 1.647, 0.832, 1.363 H, 1.792, 1.203, -1.629	5.68293, 5.36595, 3.62995	62, 258, 274, 304, 584, 871, 901, 981, 3732

190   [a] Calculated at the B3LYP/gen level of theory (see text)

The absorption cross-sections of the aforementioned molecules were calculated using the time-dependent density functional (TD-DFT) excited states method (Stratmann et al., 1998) within the Gaussian 16 suite of programs (Frisch et al., 2016). The

vertical excitation frequencies ($\tilde{v}_i$) and oscillator strengths (f_i) were obtained for the first 30 excited states. The cross section $\sigma(\tilde{v})$ at frequency $\tilde{v}$ was then computed using the GaussView program (Dennington et al., 2016):

$$\sigma(\tilde{v}) = 2.17 \times 10^{-16} \quad \sum_{i=1}^{n} \left(\frac{f_i}{\Delta} \exp\left[-\left(\frac{\tilde{v} - \tilde{v}_i}{\Delta} \right)^2 \right] \right) \tag{7}$$

where the summation is over the 30 electronic excited states and $\sigma(\tilde{v})$ is in units of cm^2 molecule^{-1}. Each peak is assumed to have a Gaussian band shape with a width Δ, set here to the default value (Dennington et al., 2016) of 0.4 eV.
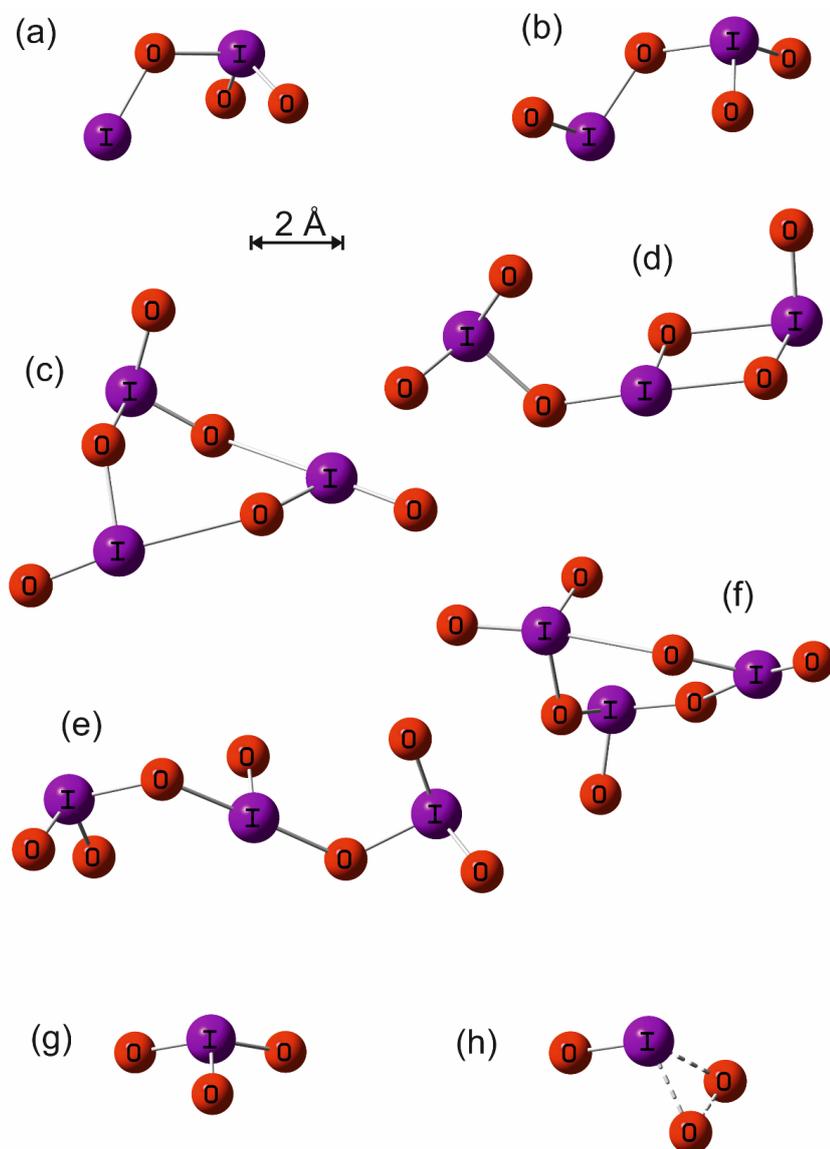
Figure 5: Molecular geometries of I$_2$O$_3$, I$_2$O$_4$, I$_3$O$_6$ (cyclic), I$_3$O$_6$ (linear), I$_3$O$_7$ (cyclic), I$_3$O$_7$ (linear), IO$_3$ and the transition state for dissociation of IO$_3$ to IO + O$_2$, calculated at the B3LYP/gen level of theory (see text for details).

2.3. Photolysis rate calculations

In this study we employ the global 3D model CAM-Chem (Community Atmospheric Model with chemistry, version 4.0),
included in the CESM framework (Community Earth System Model) (Lamarque et al., 2012), to estimate the photolysis rate
(J) of the different I_xO_y species according to their computed absorption cross-section, constrained by the experimental data at
532 and 355 nm. CAM-Chem has been configured with a 2.5° longitude by 1.9° latitude spatial resolution and 26 vertical level
(from the surface to up to 40 km). The model was run in the specified dynamics mode (Lamarque et al., 2012), using offline
meteorological fields from a previous free-running climatic simulation (Fernandez et al., 2014; Saiz-Lopez et al., 2015).
CAM-Chem implements a state-of-the-art halogen chemistry scheme (Fernandez et al., 2014; Saiz-Lopez et al., 2014; Saiz-
Lopez et al., 2015). This chemical scheme is fed by both organic and inorganic halogen emission sources (Ordóñez et al.,
2012; MacDonald et al., 2014). Saiz-Lopez and co-workers ((Saiz-Lopez et al., 2014), hereafter SL2014) conducted two sets
of simulations without and with the photolysis of I_xO_y oxides in CAM-Chem to evaluate the range of inorganic iodine loading,
partitioning and impact in the troposphere. The photolysis of I_xO_y was based on the best available knowledge at that time on
the major I_xO_y species (I_2O_2, I_2O_3 and I_2O_4) and their absorption cross sections (Gómez Martín et al., 2005; Gómez Martín et
al., 2013). In this study we run photolysis simulations and compare the J values with the new cross sections to those in SL2014.

3. Results

3.1. Photolysis at 355 nm

As described in the experimental section, kinetic profiles of the growth and removal of the target iodine oxide species were
carried out in order to define the time periods with the most suitable kinetic profiles for photolysis measurements. In the case
of IO and OIO, the photolysis delay was selected based on the location of the maxima of their kinetic profiles. Typically, this
was around 1 and 2 ms for IO and OIO respectively. IO showed a clear depletion of ~20% at 355 nm (Figure 6a) corresponding
to a cross section of $\sigma_{355\,nm,\,IO} = (1.2 \pm 0.1) \times 10^{-18}$ cm^2 molecule^{-1} (based on an average of 3 measurements) in excellent
agreement with the most recent determinations based on absorption spectroscopy (Bloss et al., 2001; Spietz et al., 2005), where
the presence of an underlying absorption corresponding to a product of reactions R2, R4, R5 or R6 was accounted for (Atkinson
et al., 2007) (Figure 6b). We consider the mutual consistency between our measurement and the most reliable determinations
of the IO cross section at 355 nm as a validation of our method for determining the absorption cross sections of I_xO_y species.
As expected, no significant depletion was observed for OIO, with an upper limit of $\sigma_{355\,nm,\,OIO} < 10^{-19}$ cm^2 molecule^{-1} based on
the noise of the mass spectrometric signal at m/z 159. No significant depletion was observed for I_2O_3 (m/z =302) at 355 nm
(Figure 7, top left), and an upper limit for the absorption cross section of $\sigma_{355\,nm,\,I2O3} < 5 \times 10^{-20}$ cm^2 molecule^{-1} was determined
based on the average noise of the I_2O_3 signal. By contrast, I_2O_4 was depleted by 355 nm photolysis by ~40% (Figure 7, top
right), corresponding to a photolysis cross-section of $\sigma_{355\,nm,\,I2O4} = (2.7 \pm 0.3) \times 10^{-18}$ cm^2 molecule^{-1} (based on an average of

2 measurements).
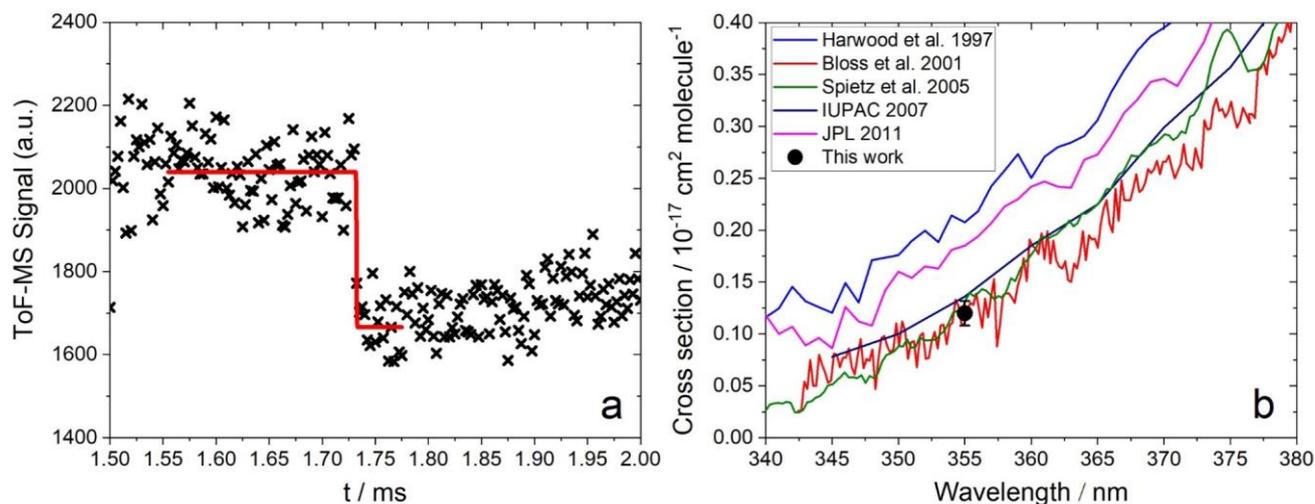
Figure 6: Panel a: measured photodepletion of IO (m/z = 143). Panel b: comparison of published absorption cross section with the absorption cross section at 355 nm determined in this work

The molecular clusters I_3O_7 (m/z = 493) and I_5O_{12} (827) are two of the major peaks of successive mass peak progressions observed in the mass spectra in Figure 3. Experimental runs with wider spectral windows show peaks that correspond to even larger molecular clusters: I_7O_{17} (1161), I_9O_{22} (1495), $I_{11}O_{27}$ (1829) and $I_{13}O_{32}$ (2163). Notably, no mass peaks with even number of iodine atoms appear. It is also interesting that these peaks are separated by 334 atomic mass units, which is the value of m/z for I_2O_5. Although I_2O_5 is not observed in the gas phase, it is noted that as the clusters grow larger, the ratio O:I ratio tends to 2.5, reaching 2.46 for $I_{13}O_{32}$, i.e. within the range of variability of the O:I ratio of iodine oxide particles (IOPs) determined by EDX (O/I = 2.42 ± 0.05) (Saunders et al., 2010). The prominent peak at m/z = 493 is the largest mass observed in our previous work on I_xO_y (Gómez Martín et al., 2013) and appears in all the spectra acquired in the course of the present work. From the observed photodepletion of I_3O_7 at 335 nm we have determined an absorption cross section of $\sigma_{355\,nm,\,I3O7}$ = (5.3 ± 1.4) × 10^{-18} cm^2 molecule^{-1} (based on an average of 3 measurements) (Figure 7). The measured cross section for the I_5O_{12} cluster is $\sigma_{355\,nm,\,I5O12}$ = (9.8 ± 1) × 10^{-18} cm^2 molecule^{-1} (based on an average of 2 measurements). The determined cross sections and upper limits at 355 nm are listed in **Table 2**.

Fragmentation precludes determination of photolysis products at 355 nm (channels of photochemical reactions R9-R11) due to the fact that the signal arising from parent ions (which may be 355 nm photolysis products), is indistinguishable from daughter ions resulting from fragmentation of higher oxides due to the 118 nm photoionization. For any given species, possible increases in signals corresponding to products of photolysis at 355 nm are offset by the decrease in the parent ion concentration and therefore the daughter ion signal. As an example, consider I_3O_7 photolysis at 355 nm. The peaks of the possible photolysis products I_2O_3, I_2O_4, OIO and IO (referred to here as photofragments), prior to photolysis will have contributions from the parent ion signals of these species, as well as daughter ion signals of I_3O_y. Upon photolysis of I_3O_7, the concentration of I_3O_7

will decrease, causing a decrease in the parent ion signal, and therefore the daughter ion signals, resulting in turn in a net negative impact on the amplitude of all daughter ion signals. In addition to the decrease in daughter ion signals resulting from

250 possible photofragment species, the parent ion signal for the photolabile species (IO, I_2O_4 in this example) will decrease due to direct photolysis of these species. Concurrently with the decrease in the I_3O_7 parent ion signal, there will be a positive contribution to some or all of the concentrations of possible photofragment parent ion signals. It is impossible to separate these contributions to the net change in signal magnitude, and therefore the products of these photolysis processes cannot be determined.

255 As indicated by reactions R10b and R11b, IO_3 ($m/z = 175$) is a potential product of I_2O_3 and I_2O_4 photolysis. However, this species has never been observed in the gas phase. According to our ab initio calculations, the ionisation potential of IO_3 is 12.1 eV, which is higher than the photoionization energy employed in the present work (10.5 eV).
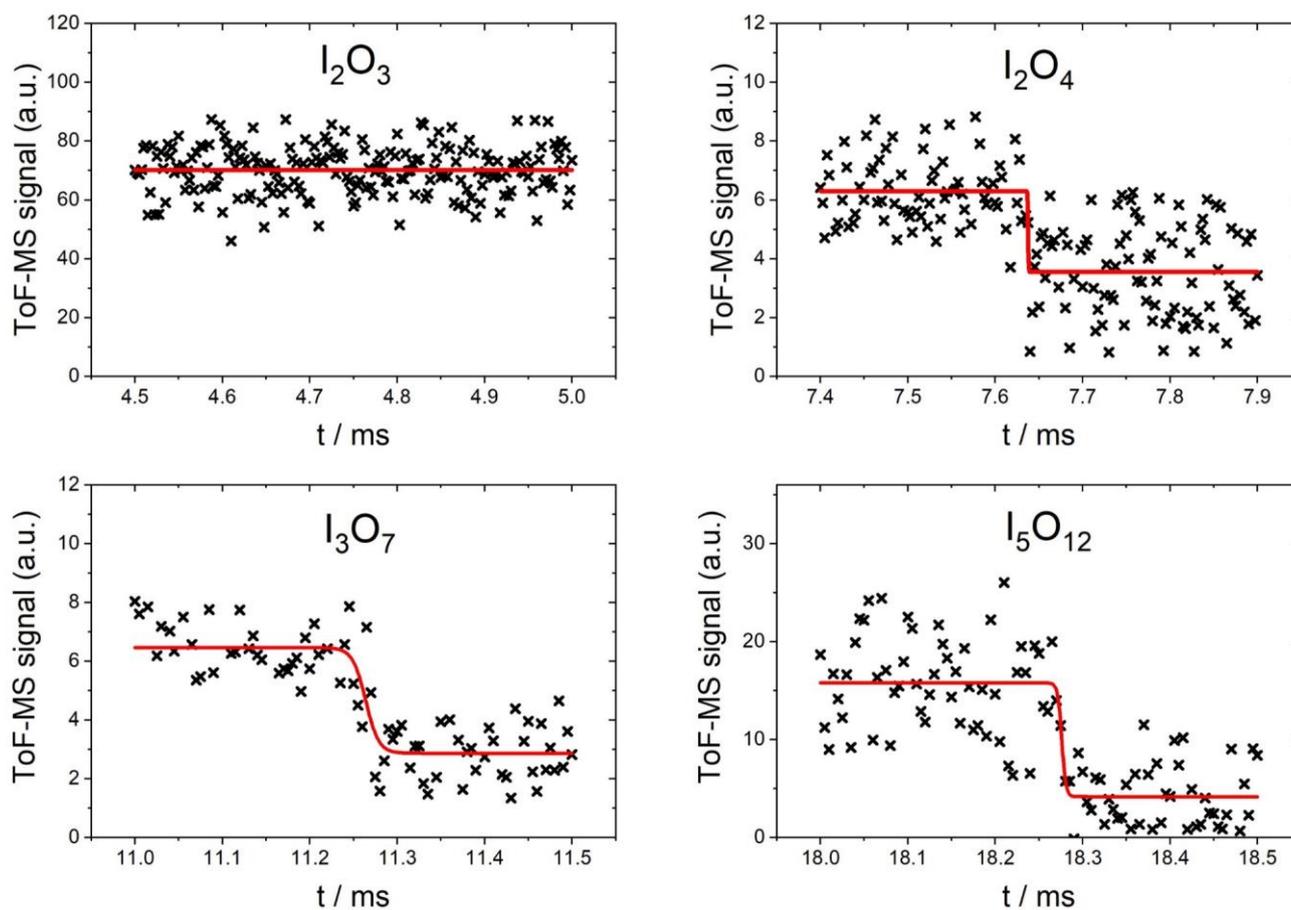
Figure 7: **Measured photodepletion at 355 nm of I_2O_3, I_2O_4, I_3O_7 and I_5O_{12}.**

3.2. Photolysis at 532 nm

As expected (Gómez Martín et al., 2009), OIO shows strong depletion in the 532 nm photolysis experiments, and it is therefore
260   used as the actinometer at this wavelength. None of the higher order iodine oxides showed measurable depletion above the
noise. Table 2 lists the upper limits to the absorption cross-sections of each species at 532 nm, determined from the signal-to-
noise ratio of the recorded traces.

Table 2: Absorption cross sections of iodine oxides at 532 nm and 355 nm

Species	$\sigma_{355\ nm}$ /cm^2 molecule^{-1}	$\sigma_{532\ nm}$/cm^2 molecule^{-1}
IO	$(1.2 \pm 0.1) \times 10^{-18}$	[a]
OIO	$< 10^{-19}$	[b]
I_2O_3	$< 5 \times 10^{-19}$	$<5.0 \times 10^{-19}$
I_2O_4	$(3.9 \pm 1.2) \times 10^{-18}$	$<1.3 \times 10^{-18}$
I_3O_6	$(6.1 \pm 1.6) \times 10^{-18}$	$<1.5 \times 10^{-18}$
I_3O_7	$(5.3 \pm 1.4) \times 10^{-18}$	$<1.4 \times 10^{-18}$
I_5O_{12}	$(9.8 \pm 1.0) \times 10^{-18}$	$<1.5 \times 10^{-18}$

[a] The 0←0 band of IO is placed at 465.5 nm (Spietz et al., 2005), and therefore, there cannot be any band of ground state IO (v" = 0) at a
265   longer wavelength. There is a hot band at ~530 nm (0←4), but the v" = 4 state is not populated at room temperature in equilibrium.
[b] Actinometer

4. Discussion

4.1. Absorption spectra

A time-dependent broad band absorption was observed by Bloss et al. (2001) concurrently with the IO self-reaction decay,
270   which was assigned to I_2O_2. The shape of the band was observed to be different for λ < 360 nm depending on the chemical
scheme employed to generate iodine oxides. Later, a broad band absorption with a similar spectral slope was reported (Figure
8) together with targeted UV measurements showing that the band peaks around 250 nm (Gómez Martín et al., 2005; Spietz
et al., 2005). The kinetics of the absorption spectrum for λ > 310 nm were found to result from the overlap of at least two
different species, one dominating the absorption below 340 nm (labelled as Y) and another one dominating from 340 nm
275   towards the visible (labelled as Z). It was found that the kinetics of species Y was compatible with a product of the IO self-
reaction, i.e. I_2O_2. By contrast Z, which would be similar to the spectrum measured by Bloss et al. for λ > 360 nm, was not
compatible with a product of the IO self-reaction, and it was tentatively assigned to I_2O_3.
Gomez Martin et al. (2005) derived the cross section of the species Y and Z at 322 nm and 356 nm respectively, using an
iodine mass conservation approach where the depletion of the I_2 precursor was balanced by the sum of atomic iodine contained
280   in the oxides formed after the photolysis flash. The cross sections were determined in a per iodine atom basis. Assuming

absorbers with two iodine atoms, the spectra of Y and Z were scaled as shown in Figure 8 (Saiz-Lopez et al., 2014). Since the spectra are featureless, they can be assumed to result from bound to free transitions, justifying a unit photolysis quantum yield of the molecules generating them.
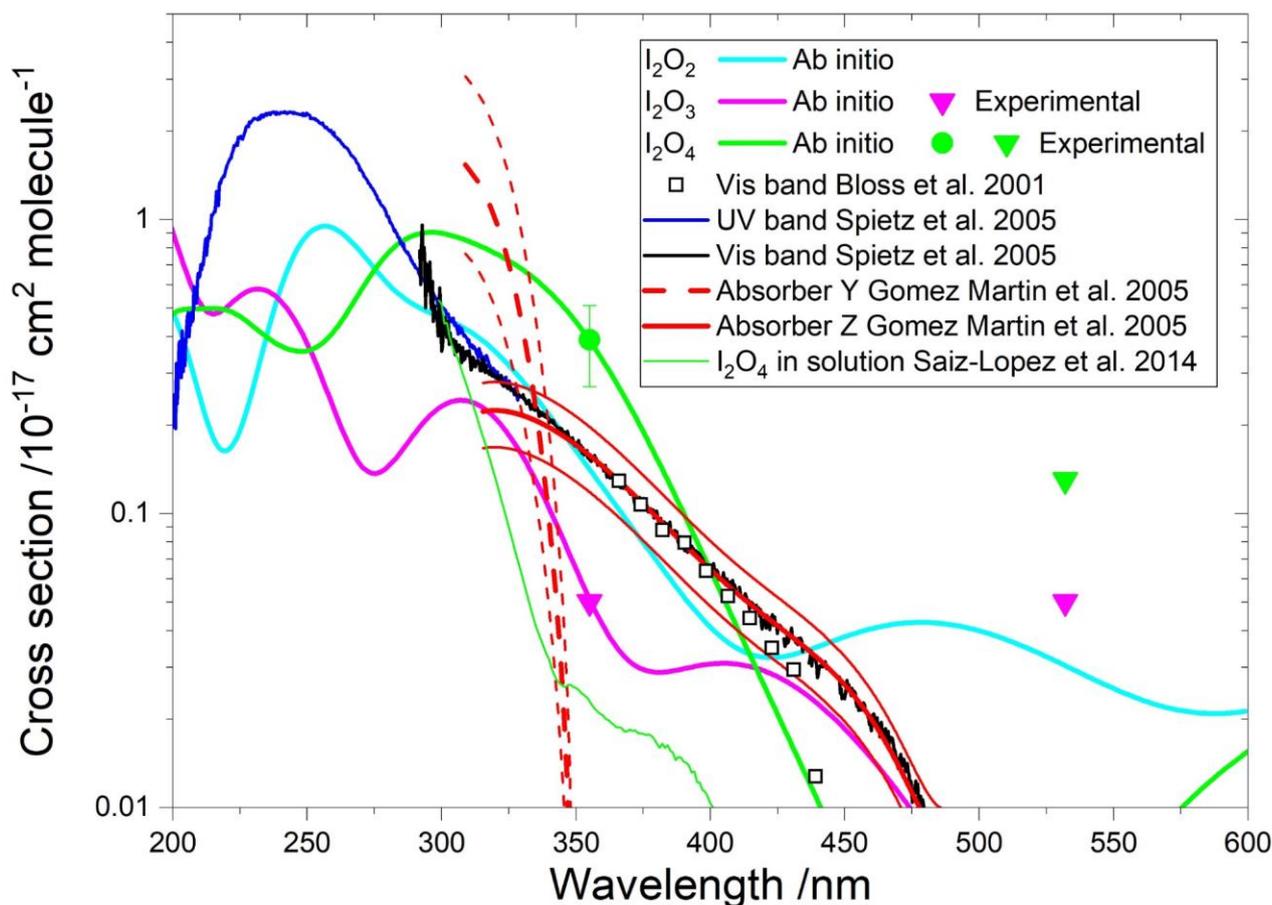
Figure 8: Absorption cross sections of I₂O₂, I₂O₃ and I₂O₄. The cyan, pink and green lines correspond to the respective ab initio spectra. The pink and green symbols indicate respectively the measured absorption cross sections of I₂O₃ and I₂O₄ (triangles indicate upper limits). The empty squares correspond to an absorption band reported by Bloss et al. (2001) in 8 nm interval averages for λ > 362 nm. The blue and black lines correspond to absorption bands reported by Spietz et al. (2005). The latter was found to be a superposition of two absorptions with different kinetic behaviour, denoted Y (dashed red line) and Z (solid red line) (Gómez Martín et al., 2005). The thin red lines represent the uncertainties of these spectra, which mainly originate from the absolute absorption cross sections of Y and Z at 322 and 356 nm respectively. A spectrum of I₂O₄ in solution is indicated in green (Saiz-Lopez et al., 2014).

The absorption cross sections determined in this work from photodepletion of I₂O₃ and I₂O₄ at 355 nm do not confirm the previous tentative assignment of absorber Z to I₂O₃. The cross section of I₂O₄ obtained from our photodepletion experiments is in better agreement with the absorber Z. Also, it appears that the spectrum of I₂O₄ in solution largely underestimates the gas-phase spectrum. The absorption of Z at 355 nm in Figure 8 lies slightly below the I₂O₄ cross section determined in the present

work, which is consistent with a contribution to Z of other I_xO_y species with $x > 2$ (i.e. the scaling of the spectrum should be effectively higher than the factor of 2 used by Gomez Martin et al. (2005)). In fact, the theoretical spectra of I_2O_4, I_3O_6 and

290   I_3O_7 (Figure 8 and Figure 9) show similar shapes between 300 and 500 nm. It is very likely that the absorption band extending from 200 nm to nearly 500 nm (blue and black lines in Figure 8) results from the overlap of absorptions corresponding to several I_xO_y species. Therefore, these experimental absorption spectra are not useful for photolysis rates calculations unless
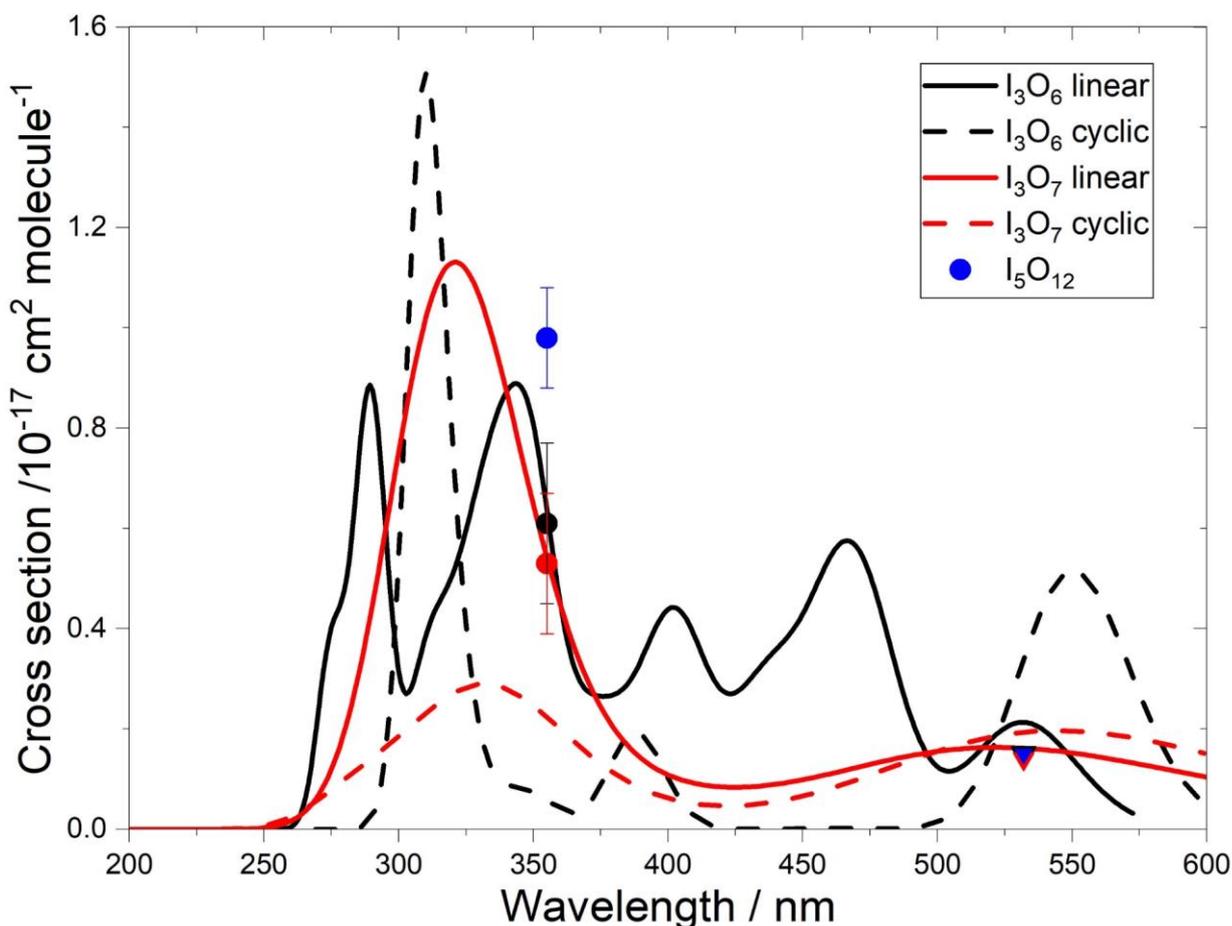
Figure 9: Absorption cross section spectra of I₃O₆ (black lines and symbols), I₃O₇ (red lines and symbols) and I₅O₁₂ (blue symbols). Ab initio spectra of linear and cyclic isomers are shown by solid and dashed lines, respectively.

further deconvolution enables separation of the different contributions.

The calculated spectra shown in Figure 8 and Figure 9 agree generally well with the experimentally determined values at 355

295   nm and 532 nm, with only the upper limits for I_3O_6 and I_3O_7 appearing to be below the calculated values at 532 nm. Note that theoretical absorption cross section spectra for both the linear and cyclic forms (Figure 5) of I_3O_6 and I_3O_7 are shown in Figure 9. The linear forms of both species fit significantly better to the experimental values, suggesting the linear form is the one which is formed preferentially in these reactions.

4.2. Photolysis products

300 The likely photodissociation pathways of I_2O_3 and I_2O_4 can be elucidated by seeing how the geometry of each excited state relaxes after vertical excitation from the ground-state geometry using the TD-DFT method (see Section 2.2). In the case of I_2O_3, excitation in both the bands at 334 and 453 nm (Figure 8) produces a pronounced extension of the I–IO_3 bond, indicating photolysis leading to I + IO_3 (R10b). For I_2O_4, excitation at 667 nm and in its strong band at 324 nm produces IO + IO_3, whereas absorption in the weak band at 366 nm produces OIO + OIO.
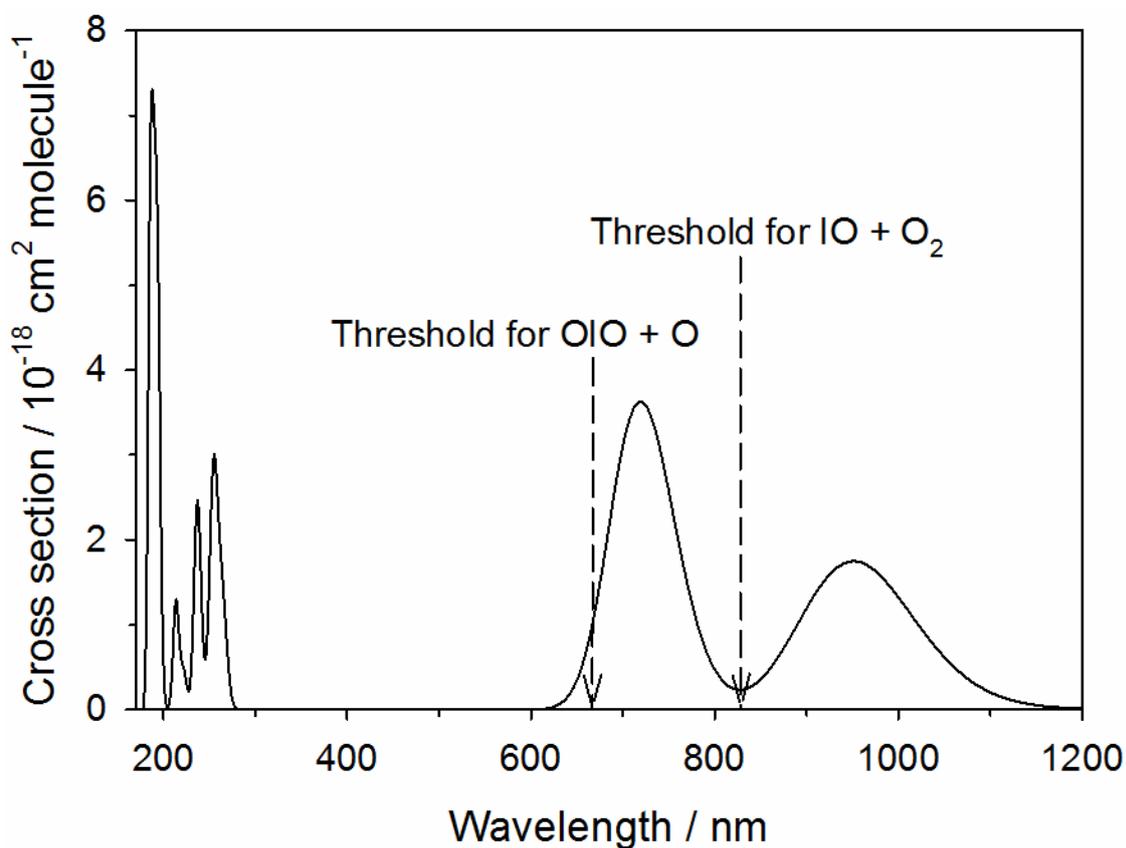
Figure 10: Absorption spectrum of IO$_3$ calculated at the TD/B3LYP/gen level of theory (see text for further details). The arrows indicate the energy thresholds for the two photodissociation pathways.

305 The theoretical absorption spectrum of IO_3 is shown in Figure 10, calculated at the same level of theory as described in Section 2.2. IO_3 absorbs in the tropospheric solar actinic range in two near-IR bands centered at 710 and 950 nm. There are two possible photolysis pathways:

$$IO_3 + h\nu \rightarrow OIO + O \tag{R15}$$

$$\rightarrow IO + O_2 \tag{R16}$$

310   The first channel requires 180 kJ mol^{-1} to break the O_2I–O bond (not including spin-orbit coupling), corresponding to a photolytic threshold of 665 nm. R16 is closely analogous to the photolysis of OIO in its band between 500 and 600 nm, where the I atom is squeezed out from between the two O atoms in a process that overall is actually exothermic because of the strength of the newly-formed O_2 bond (Gómez Martín et al., 2009). In the same way, R16 is exothermic by 78 kJ mol^{-1}. However, there is a barrier of 145 kJ mol^{-1} involved in squeezing the IO out from between the 2 oxygen atoms. This corresponds to a photolytic

315   threshold of 827 nm. Both of these thresholds are indicated on Figure 10. This shows that absorption across the entire 710 nm band is sufficient for photolysis via R16 to occur. If that were the case, then $J(IO_3 \rightarrow IO + O_2)$ could be as large as 0.15 s^{-1}. Photolysis via R15 is just possible in the short wavelength tail of the 710 nm band, so $J(IO_3 \rightarrow OIO + O)$ could be as large as 0.007 s^{-1}. It therefore seems likely that photolysis of IO_3 is fast and mainly produces IO.
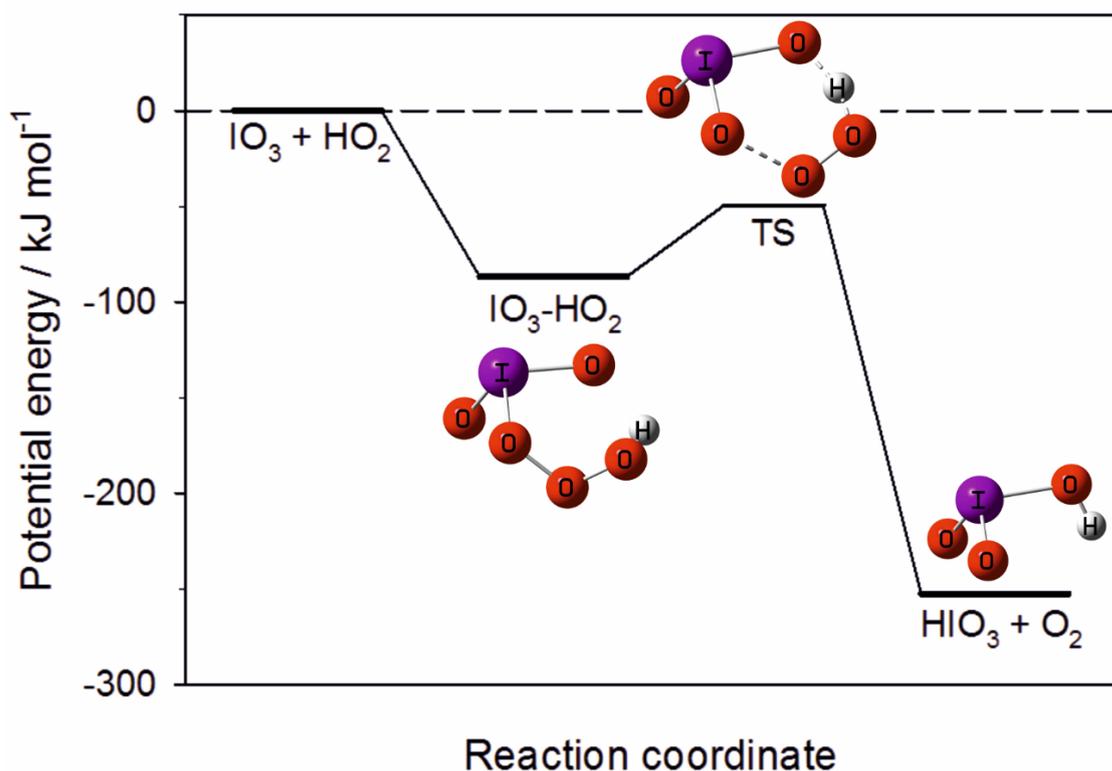
Figure 11: Potential energy surface for the reaction between IO_3 and HO_2 to produce HIO_3, calculated at the B3LYP/gen level of theory (see text for further details).

If, however, photolysis of IO_3 is significantly slower than this upper limit, the molecule could persist in the atmosphere long

320   enough to undergo reaction with other molecules. An intriguing possibility is that IO_3 may be a source of HIO_3. The reaction

$$IO_3 + H_2O \rightarrow HIO_3 + OH \hspace{6cm} (R16)$$

is endothermic by 25 kJ mol^{-1} (14 kJ mol^{-1} according to previous work at higher level of theory (Khanniche et al., 2017b)),

and so most likely does not occur. However, the reaction

$$IO_3 + HO_2 \rightarrow HIO_3 + O_2 \hspace{5cm} (R17)$$

325 is very exothermic with a deep submerged barrier (Figure 11). A Rice-Ramsperger-Kassel-Markus (RRKM) calculation using the MESMER program (Glowacki et al., 2012) with the molecular parameters in Table 1 indicates that the rate constant of R17 is $k(290\ K) \sim 3 \times 10^{-11}$ cm^3 molecule^{-1} s^{-1}. Given that [HO$_2$] is typically 3×10^8 molecule cm^{-3} at midday (Stone et al., 2012), IO$_3$ could be converted to HIO$_3$ with a reaction rate of ~ 0.01 s^{-1} i.e. about 15 times slower than the upper limit to the photolysis rate discussed above. R17 could therefore provide a route to HIO$_3$ formation, and this should be the subject of future
330 investigation.

4.3. Atmospheric implications

The theoretical spectra constrained with the measurements at 355 nm and 532 nm have been implemented in CAM-Chem in order to calculate photolysis rates for I$_2$O$_y$ (y = 2, 3, 4) and I$_3$O$_7$. The main changes with respect to SL2014 are:

1. The new I$_2$O$_2$ cross sections are lower in the UV than those of the absorber Y used in SL2014 (Figure 8) and extend
335 over a wider range of the actinic range.

2. I$_2$O$_3$ and I$_2$O$_4$ have respectively lower and higher absorption cross sections than in SL2014, as a result of replacing the absorption Z and the I$_2$O$_4$ spectrum in solution in favour of theoretical spectra constrained with experimental values. The cross section of I$_2$O$_3$ is lower, but only by a factor of ~2 in the important region between 350 nm and 450 nm. The cross sections of I$_2$O$_4$ increase by 1 order of magnitude with respect to the spectrum in solution.

340 3. Higher iodine oxides like I$_3$O$_7$ and I$_5$O$_{12}$ not included in SL2014 also photolyze. They show bands in the green part of the spectrum (Figure 9) and therefore have higher photolysis rates than I$_2$O$_4$.

Annual zonal-average photolysis rate plots are shown in Figure 12 and Figure 13. Surface atmospheric photolysis of all the I$_x$O$_y$ species is generally fastest between 30° and -30° latitude, displaying slight minima at 5° and -5° latitude due to attenuation
345 of actinic flux by cloud cover at the intertropical convergence zone. Average I$_x$O$_y$ global J values in the upper troposphere exhibit a maximum around 5° latitude, where solar flux is highest. At 5° latitude, I$_2$O$_2$ and I$_2$O$_4$ J values are largest at an altitude of 8 km. Similarly, the J values for I$_2$O$_3$ and I$_3$O$_7$ at 5° latitude are highest at 8 km, and then remain relatively constant above 20 km. In contrast with J values for I$_x$O$_y$ at 5° latitude, values at mid-latitudes increase with altitude, showing no maxima at 8 km. The observed increase in J values at 8 km is explained by the albedo effect of cloud cover in certain regions,
350 particularly the intertropical convergence zone, contributing to the total (incident + reflected) solar flux in these regions.
Figure 12(d-f) show the percentage difference between the SL2014 J values and those calculated in this study. As a result of the new I$_2$O$_2$ cross sections extending across the actinic window, this species shows an increase in J values at all latitudes, with the largest increases seen at the poles (~300% increase), and lower increases of around 100% near the equator. I$_2$O$_3$ shows a uniform decrease of around 46% across all latitudes and altitudes, as expected from the approximately uniform decrease of the

355   new spectrum with respect to absorber Z, which was taken as I_2O_3 in SL2014. I_2O_4 exhibits the largest increase in *J* values across all latitudes, ranging from 750% at 40 km between -30° and 30° latitude, up to increases above 1000% at the poles.
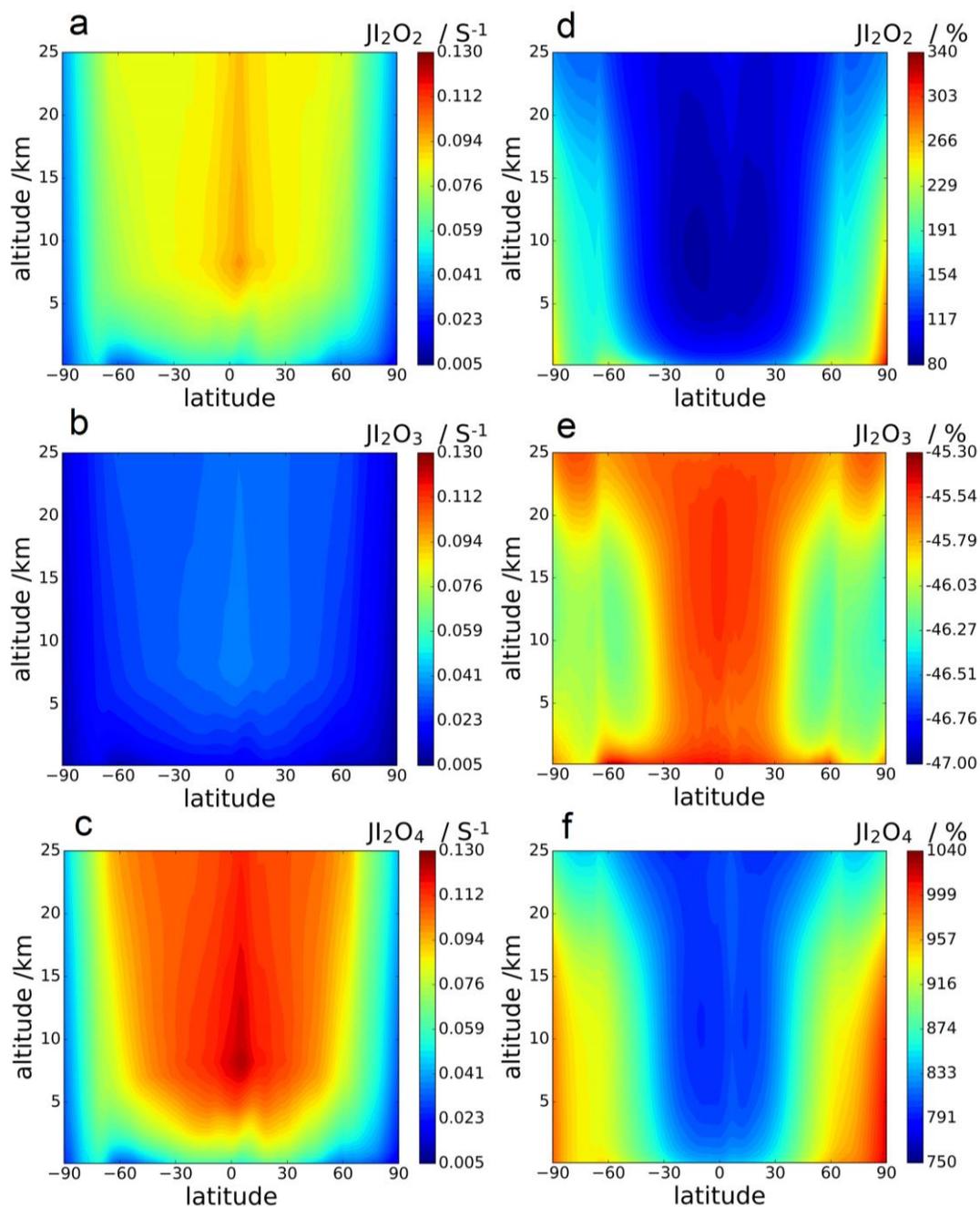
Figure 12: Annual zonal average J value vertical profiles for I_2O_2, I_2O_3 and I_2O_4 (panels a, b and c, respectively; note that the colour scale is the same for these three panels) and the percentage change between the SL2014 annual zonal average J value vertical profiles, and the profiles in this study (panels d, e and f, respectively)

Photolytic lifetimes of I_xO_y species in the troposphere vary from a few seconds for the most photolabile species, i.e. I_3O_7, to several minutes for I_2O_3, which has the smallest absorption cross-sections in the actinic region and the smallest J values of the species in this study. Mid and high-latitudes exhibit particularly low J surface values and encompass many coastal regions

360 where active iodine concentrations are high and iodine-driven particle formation has been reported (Saiz-Lopez et al., 2012b). Photolysis of higher iodine oxides (R9-R11) competes with gas-to-particle formation (R7) and recycles IO_x, which participates in ozone depleting cycles (e.g. R1-R3). Therefore, higher J values at the surface tend to hinder particle formation and enhance ozone depletion. The new spectra result in decreased photolysis lifetimes of I_2O_2 (factor of ~3) and I_2O_4 (factor of ~10) and indicate that photolysis of nascent iodine clusters such as I_3O_7 and I_5O_{12} may further slow down particle formation. On the

365 other hand, the lifetime I_2O_3 is approximately doubled, which increases the chances of participating in other reactions, including clustering with other I_xO_y. Whether this may balance the decrease in the photolysis lifetimes of other species or not remains to be studied in future work. I_2O_3 is believed to be an important iodine reservoir and key intermediate in the formation of new particles (Gómez Martín et al., 2013; Saiz-Lopez et al., 2014), but there is a substantial lack of mechanistic information about iodine oxides and how they may convert (or not) into HIO_3.
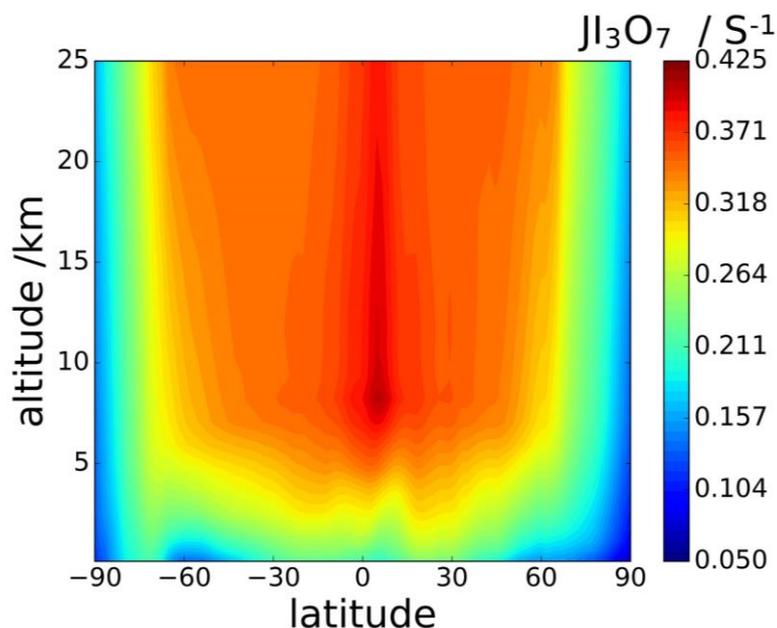
Figure 13: Annual zonal average vertical J value profile for I_3O_7 (not included in SL2014)

370 Another hotspot of iodine chemistry is the tropical upper troposphere - lower stratosphere region (UTLS), where significant concentrations of iodine exist as a result of strong convection carrying iodine precursors emitted at the ocean surface (mainly CH_3I). The effect of the new spectra on the J values in this region is similar to the effect at the surface, although the changes are less pronounced. In the UTLS, I_xO_y molecules play the role of iodine reservoirs and, as a result of the enhanced actinic flux (see J maxima between 8 and 17 km around the equator in Figures 12 and 13), their photolysis has a significant impact

375 on ozone depletion in this climatically sensitive region (Saiz-Lopez et al., 2012a). Iodine recycling in aerosol is believed to

play an important role in explaining observed concentrations of gas-phase IO_x (Koenig et al., 2020). The form in which gas-phase iodine (oxides, oxyacids or nitrate) is taken up in sulphate aerosol may also determine the extent to which iodine can return to the gas phase.

To investigate with more detail the effect of the new spectra on particle formation, iodine speciation in aerosol and ozone
380 depletion, the iodine chemistry scheme in CAM-Chem needs to be expanded to include the photolysis products and yields of I_xO_y photolysis reactions, as well as the reactions of the possible photoproducts, which are poorly known. New laboratory and theoretical work is required to solve these uncertainties. The mechanism of IOP formation remains controversial, with two possible pathways proposed via I_xO_y and HIO_3. Work on the IOP formation mechanism conducted in the course of this research will be published elsewhere. Future laboratory measurements of I_xO_y spectra and kinetics may benefit from a multiplexed
385 approach where tuneable photoionization mass spectrometry, absorption spectroscopy and multi-wavelength laser photodepletion are used concurrently. A follow up modelling study will be conducted with an updated mechanism for atmospheric iodine chemistry, including the photochemistry outlined in this paper, as well as a chemical scheme for IOP formation.

5. Conclusion

390 The photodepletion laboratory experiments reported in this work confirm that I_xO_y species are photolabile, and therefore supports the $J(I_xO_y)$ scenario in ASL2014, with important consequences for ozone depletion. The values of the absorption cross sections obtained at 355 nm and 532 nm have been employed to revisit the assignment of absorption bands in previous work. Also, comparison between theoretical spectra and measurements gives some clues about the geometry of the molecules. I_2O_3 has a smaller absorption cross-section in the actinic region than previously thought, which may facilitate other reactions,
395 including clustering to form new particles. Other I_xO_y species have larger absorption cross-sections in the actinic region, resulting in rapid photolysis to smaller iodine-containing molecules. Possible photolysis products include IO_3, which could be a precursor of HIO_3 in the marine boundary layer. These new findings highlight the need for new experimental and theoretical studies, particularly investigating the products of these photochemical processes, as well as the effect on IOPs (and therefore cloud condensation nuclei) formation.

400 **Author contribution.** A. S.-L. devised the research. J. C. G. M., M. A. B. and J. M. C. P. designed the experimental set up, and T. R. L. carried out the experiments and analysed the data; J. M. C. P. and J. C. G. M. carried out electronic structure and master equation calculations; C. A. C. carried out radiative transfer calculations; T. R. L. and J. C. G. M. wrote the manuscript with contributions from all co-authors.

Competing interests. The authors declare that they have no conflict of interest.

405 **Acknowledgements.** This study has received funding from the European Research Council Executive Agency under the European Union's Horizon 2020 Research and Innovation program (Project 'ERC-2016-COG 726349 CLIMAHAL'). J. C. G. M. acknowledges financial support from the State Agency for Research of the Spanish MCIU through the "Center of

Excellence Severo Ochoa" award to the Instituto de Astrofísica de Andalucía (SEV-2017-0709) and the Ramon y Cajal
program (RYC-2016-19570). J. C. G. M. and A. S.-L. acknowledge support of the publication fee by the CSIC Open Access
410 Publication Support Initiative through its Unit of Information Resources for Research (URICI).

References

Atkinson, R., Baulch, D. L., Cox, R. A., Crowley, J. N., Hampson, R. F., Hynes, R. G., Jenkin, M. E., Rossi, M. J., and Troe, J.: Evaluated kinetic and photochemical data for atmospheric chemistry: Volume III – gas phase reactions of inorganic halogens, Atmos. Chem. Phys., 7, 981-1191, doi: 10.5194/acp-7-981-2007, 2007.

415 Bloss, W. J., Rowley, D. M., Cox, R. A., and Jones, R. L.: Kinetics and Products of the IO Self-Reaction, J. Phys. Chem. A, 105, 7840-7854, doi: 10.1021/jp0044936, 2001.

Burkholder, J. B., Sander, S. P., Abbat, J., Barker, J. R., Huie, R. E., Kolb, C. E., Kurylo, M. J., Orkin, V. L., Wilmouth, D. M., and Wine, P. H.: Chemical Kinetics and Photochemical Data for Use in Atmospheric Studies, Evaluation No. 18 JPL-NASA, Pasadena, 2015.

420 Burrows, J., Richter, A., Dehn, A., Deters, B., Himmelmann, S., Voigt, S., and Orphal, J.: Atmospheric remote-sensing reference data from GOME—2. Temperature-dependent absorption cross sections of O3 in the 231–794 nm range, J. Quant. Spectrosc. Radiat. Transfer, 61, 509-517, doi: 10.1016/S0022-4073(98)00037-5, 1999.

Canneaux, S., Xerri, B., Louis, F., and Cantrel, L.: Theoretical Study of the Gas-Phase Reactions of Iodine Atoms (2P3/2) with H2, H2O, HI, and OH, J. Phys. Chem. A, 114, 9270-9288, doi: 10.1021/jp104163t, 2010.

425 Carpenter, L. J., MacDonald, S. M., Shaw, M. D., Kumar, R., Saunders, R. W., Parthipan, R., Wilson, J., and Plane, J. M. C.: Atmospheric iodine levels influenced by sea surface emissions of inorganic iodine, Nat. Geosci., 6, 108-111, doi: 10.1038/ngeo1687, 2013.

Chance, R., Baker, A. R., Carpenter, L., and Jickells, T. D.: The distribution of iodide at the sea surface, Environ. Sci. Process Impacts, 16, 1841-1859, doi: 10.1039/c4em00139g, 2014.

430 Cox, R. A., and Coker, G. B.: Absorption Cross section and Kinetics of IO in the Photolysis of CH$_3$I in the presence of Ozone, J. Phys. Chem., 87, 4478-4484., doi: 10.1021/j100245a030, 1983.

Cuevas, C. A., Maffezzoli, N., Corella, J. P., Spolaor, A., Vallelonga, P., Kjær, H. A., Simonsen, M., Winstrup, M., Vinther, B., Horvat, C., Fernandez, R. P., Kinnison, D., Lamarque, J.-F., Barbante, C., and Saiz-Lopez, A.: Rapid increase in atmospheric iodine levels in the North Atlantic since the mid-20th century, Nat. Commun., 9, 1452, doi: 435 10.1038/s41467-018-03756-1, 2018.

Dennington, R., Keith, T. A., and Millam, J. M.: GaussView, Version 6.1, Semichem Inc., Shawnee Mission, KS, 2016.

Fernandez, R. P., Salawitch, R., Kinnison, D., Lamarque, J.-F., and Saiz-lopez, A.: Bromine partitioning in the tropical tropopause layer: implications for stratospheric injection, Atmos. Chem. Phys., doi: 10.5194/acp-14-13391-2014, 2014.

440   Frisch, M. J., Trucks, G. W., Schlegel, H. B., Scuseria, G. E., Robb, M. A., Cheeseman, J. R., Scalmani, G., Barone, V., Petersson, G. A., Nakatsuji, H., Li, X., Caricato, M., Marenich, A. V., Bloino, J., Janesko, B. G., Gomperts, R., Mennucci, B., Hratchian, H. P., Ortiz, J. V., Izmaylov, A. F., Sonnenberg, J. L., Williams-Young, D., Ding, F., Lipparini, F., Egidi, F., Goings, J., Peng, B., Petrone, A., Henderson, T., Ranasinghe, D., Zakrzewski, V. G., J. Gao, N. R., Zheng, G., Liang, W., Hada, M., Ehara, M., Toyota, K., Fukuda, R., Hasegawa, J., Ishida, M., Nakajima, T.,
445   Honda, Y., Kitao, O., Nakai, H., Vreven, T., Throssell, K., J. A. Montgomery, J., Peralta, J. E., Ogliaro, F., Bearpark, M. J., Heyd, J. J., Brothers, E. N., Kudin, K. N., Staroverov, V. N., Keith, T. A., Kobayashi, R., Normand, J., Raghavachari, K., Rendell, A. P., Burant, J. C., Iyengar, S. S., Tomasi, J., Cossi, M., Millam, J. M., Klene, M., Adamo, C., Cammi, R., Ochterski, J. W., Martin, R. L., Morokuma, K., Farkas, O., Foresman, J. B., and Fox, D. J.: Gaussian 16, Revision B.01, Gaussian, Inc., Wallingford, CT, USA, 2016.

450   Galvez, O., Gómez Martín, J. C., Gomez, P. C., Saiz-Lopez, A., and Pacios, L. F.: A theoretical study on the formation of iodine oxide aggregates and monohydrates, Phys. Chem. Chem. Phys., 15, 15572-15583, doi: 10.1039/c3cp51219c, 2013.

Glowacki, D. R., Liang, C.-H., Morley, C., Pilling, M. J., and Robertson, S. H.: MESMER: An Open-Source Master Equation Solver for Multi-Energy Well Reactions, J. Phys. Chem. A, 116, 9545-9560, doi: 10.1021/jp3051033, 2012.

455   Glukhovtsev, M. N., Pross, A., McGrath, M. P., and Radom, L.: Extension of Gaussian-2 (G2) theory to bromine- and iodine-containing molecules: Use of effective core potentials, J. Chem. Phys., 103, 1878-1885, doi: 10.1063/1.469712, 1995.

Gómez Martín, J. C., Spietz, P., and Burrows, J. P.: Spectroscopic studies of the I_2/O_3 photochemistry: Part 1: Determination of the absolute absorption cross sections of iodine oxides of atmospheric relevance, J. Photochem. Photobiol., A, 176, 15-38, doi: 10.1016/j.jphotochem.2005.09.024, 2005.

460   Gómez Martín, J. C., Spietz, P., and Burrows, J. P.: Kinetic and Mechanistic Studies of the I_2/O_3 Photochemistry, J. Phys. Chem. A, 111, 306-320, doi: 10.1021/jp061186c, 2007.

Gómez Martín, J. C., Ashworth, S. H., Mahajan, A. S., and Plane, J. M. C.: Photochemistry of OIO: Laboratory study and atmospheric implications, Geophys. Res. Lett., 36, L09802, doi: 10.1029/2009GL037642, 2009.

Gómez Martín, J. C., Galvez, O., Baeza-Romero, M. T., Ingham, T., Plane, J. M. C., and Blitz, M. A.: On the mechanism of
465   iodine oxide particle formation, Phys. Chem. Chem. Phys., 15, 15612-15622, doi: 10.1039/c3cp51217g, 2013.

Gómez Martín, J. C., Garraway, S. A., and Plane, J. M. C.: Reaction Kinetics of Meteoric Sodium Reservoirs in the Upper Atmosphere, J. Phys. Chem. A, 120, 1330-1346, doi: 10.1021/acs.jpca.5b00622, 2016.

Hammaecher, C., Canneaux, S., Louis, F., and Cantrel, L.: A Theoretical Study of the H-Abstraction Reactions from HOI by Moist Air Radiolytic Products (H, OH, and O (3P)) and Iodine Atoms (2P3/2), J. Phys. Chem. A, 115, 6664-6674,
470   doi: 10.1021/jp202760u, 2011.

Harwood, M. H., Burkholder, J. B., Hunter, M., Fox, R. W., and Ravishankara, A. R.: Absorption Cross Sections and Self-Reaction Kinetics of the IO Radical, J. Phys. Chem. A, 101, 853-863, doi: 10.1021/jp962429b, 1997.

Hoffmann, T., O'Dowd, C. D., and Seinfeld, J. H.: Iodine oxide homogeneous nucleation: An explanation for coastal new particle production, Geophys. Res. Lett., 28, 1949-1952, doi: 10.1029/2000GL012399, 2001.

475 Jimenez, J. L., Bahreini, R., Cocker, D. R., III, Zhuang, H., Varutbangkul, V., Flagan, R. C., Seinfeld, J. H., O'Dowd, C. D., and Hoffmann, T.: New particle formation from photooxidation of diiodomethane (CH_2I_2), J. Geophys. Res. [Atmos.], 108, 4318, doi: 10.1029/2002JD002452, 2003.

Khanniche, S., Louis, F., Cantrel, L., and Černušák, I.: Thermochemistry of HIO_2 Species and Reactivity of Iodous Acid with OH Radical: A Computational Study, ACS Earth Space Chem., 1, 39-49, doi: 10.1021/acsearthspacechem.6b00010,
480 2017a.

Khanniche, S., Louis, F., Cantrel, L., and Černušák, I.: Investigation of the Reaction Mechanism and Kinetics of Iodic Acid with OH Radical Using Quantum Chemistry, ACS Earth Space Chem., 1, 227-235, doi: 10.1021/acsearthspacechem.7b00038, 2017b.

Koenig, T. K., Baidar, S., Campuzano-Jost, P., Cuevas, C. A., Dix, B., Fernandez, R. P., Guo, H., Hall, S. R., Kinnison, D.,
485 Nault, B. A., Ullmann, K., Jimenez, J. L., Saiz-Lopez, A., and Volkamer, R.: Quantitative detection of iodine in the stratosphere, Proc. Nat. Acad. Sci. U.S.A., 117, 1860-1866, doi: 10.1073/pnas.1916828117, 2020.

Kumar, M., Saiz-Lopez, A., and Francisco, J. S.: Single-Molecule Catalysis Revealed: Elucidating the Mechanistic Framework for the Formation and Growth of Atmospheric Iodine Oxide Aerosols in Gas-Phase and Aqueous Surface Environments, J. Am. Chem. Soc., 140, 14704-14716, doi: 10.1021/jacs.8b07441, 2018.

490 Kung, A. H., Young, J. F., and Harris, S. E.: Generation of 1182-Å radiation in phase-matched mixtures of inert gases, Appl. Phys. Lett., 22, 301-302, doi: 10.1063/1.1654647, 1973.

Lamarque, J.-F., Emmons, L., Hess, P., Kinnison, D. E., Tilmes, S., Vitt, F., Heald, C., Holland, E. A., Lauritzen, P., and Neu, J.: CAM-chem: Description and evaluation of interactive atmospheric chemistry in the Community Earth System Model, Geosci. Model Dev., 5, 369, doi: 10.5194/gmd-5-369-2012, 2012.

495 Laszlo, B., Kurylo, M. J., and Huie, R. E.: Absorption cross sections, kinetics of formation, and self-reaction of the IO radical produced via the laser photolysis of $N_2O/I_2/N_2$ mixtures, J. Phys. Chem., 99, 11701-11707, doi: 10.1021/j100030a013, 1995.

Lewis, T., Heard, D. E., and Blitz, M. A.: A novel multiplex absorption spectrometer for time-resolved studies, Rev. Sci. Instrum., 89, 024101, doi: 10.1063/1.5006539, 2018.

500 MacDonald, S. M., Gómez Martín, J. C., Chance, R., Warriner, S., Saiz-Lopez, A., Carpenter, L. J., and Plane, J. M. C.: A laboratory characterisation of inorganic iodine emissions from the sea surface: dependence on oceanic variables and parameterisation for global modelling, Atmos. Chem. Phys., 14, 5841-5852, doi: 10.5194/acp-14-5841-2014, 2014.

Mahon, R., McIlrath, T., Myerscough, V., and Koopman, D.: Third-harmonic generation in argon, krypton, and xenon: Bandwidth limitations in the vicinity of Lyman-α, IEEE J. Quantum Electron., 15, 444-451, doi:
505 10.1109/jqe.1979.1070036, 1979.

McFiggans, G., Coe, H., Burgess, R., Allan, J., Cubison, M., Alfarra, M. R., Saunders, R., Saiz-Lopez, A., Plane, J. M. C., Wevill, D. J., Carpenter, L. J., Rickard, A. R., and Monks, P. S.: Direct evidence for coastal iodine particles from Laminaria macroalgae - linkage to emissions of molecular iodine, Atmos. Chem. Phys., 4, 701-713, doi: 10.5194/acp-4-701-2004, 2004.

510 Ordóñez, C., Lamarque, J.-F., Tilmes, S., Kinnison, D. E., Atlas, E. L., Blake, D. R., Sousa Santos, G., Brasseur, G., and Saiz-Lopez, A.: Bromine and iodine chemistry in a global chemistry-climate model: description and evaluation of very short-lived oceanic sources, Atmos. Chem. Phys., 12, 1423-1447, doi: 10.5194/acp-12-1423-2012, 2012.

Pirjola, L., O'Dowd, C., Yoon, Y. J., and Sellegri, K.: Modelling Iodine Particle Formation and Growth from Seaweed in a Chamber, Environ. Chem., 2, 271-281, doi: 10.1071/EN05075, 2005.

515 Prados-Roman, C., Cuevas, C. A., Fernandez, R. P., Kinnison, D. E., Lamarque, J. F., and Saiz-Lopez, A.: A negative feedback between anthropogenic ozone pollution and enhanced ocean emissions of iodine, Atmos. Chem. Phys., 15, 2215-2224, doi: 10.5194/acp-15-2215-2015, 2015.

Saiz-Lopez, A., and Plane, J. M. C.: Novel iodine chemistry in the marine boundary layer, Geophys. Res. Lett., 31, L04112, doi: 10.1029/2003GL019215, 2004.

520 Saiz-Lopez, A., Saunders, R., Joseph, D., Ashworth, S., and Plane, J.: Absolute absorption cross-section and photolysis rate of I 2, Atmos. Chem. Phys., 4, 1443-1450, doi: 10.5194/acp-4-1443-2004, 2004.

Saiz-Lopez, A., Lamarque, J. F., Kinnison, D. E., Tilmes, S., Ordóñez, C., Orlando, J. J., Conley, A. J., Plane, J. M. C., Mahajan, A. S., Sousa Santos, G., Atlas, E. L., Blake, D. R., Sander, S. P., Schauffler, S., Thompson, A. M., and Brasseur, G.: Estimating the climate significance of halogen-driven ozone loss in the tropical marine troposphere, 525 Atmos. Chem. Phys., 12, 3939-3949, doi: 10.5194/acp-12-3939-2012, 2012a.

Saiz-Lopez, A., Plane, J. M., Baker, A. R., Carpenter, L. J., von Glasow, R., Martin, J. C., McFiggans, G., and Saunders, R. W.: Atmospheric chemistry of iodine, Chem. Rev., 112, 1773-1804, doi: 10.1021/cr200029u, 2012b.

Saiz-Lopez, A., Fernandez, R. P., Ordóñez, C., Kinnison, D. E., Gómez Martín, J. C., Lamarque, J. F., and Tilmes, S.: Iodine chemistry in the troposphere and its effect on ozone, Atmos. Chem. Phys., 14, 13119-13143, doi: 10.5194/acp-14-530 13119-2014, 2014.

Saiz-Lopez, A., Baidar, S., Cuevas, C. A., Koenig, T., Fernandez, R. P., Dix, B., Kinnison, D. E., Lamarque, J.-F., Rodriguez-Lloveras, X., and Campos, T. L.: Injection of iodine to the stratosphere, Geophys. Res. Lett., 42, 6852-6859, doi: 10.1002/2015GL064796, 2015.

Saunders, R. W., Mahajan, A. S., Gómez Martín, J. C., Kumar, R., and Plane, J. M. C.: Studies of the Formation and Growth 535 of Aerosol from Molecular Iodine Precursor, Z. Phys. Chem., 224, 1095-1117, doi: 10.1524/zpch.2010.6143, 2010.

Sherwen, T., Evans, M. J., Carpenter, L. J., Andrews, S. J., Lidster, R. T., Dix, B., Koenig, T. K., Sinreich, R., Ortega, I., Volkamer, R., Saiz-Lopez, A., Prados-Roman, C., Mahajan, A. S., and Ordóñez, C.: Iodine's impact on tropospheric oxidants: a global model study in GEOS-Chem, Atmos. Chem. Phys., 16, 1161-1186, doi: 10.5194/acp-16-1161-2016, 2016.

540   Sipilä, M., Sarnela, N., Jokinen, T., Henschel, H., Junninen, H., Kontkanen, J., Richters, S., Kangasluoma, J., Franchin, A., Peräkylä, O., Rissanen, M. P., Ehn, M., Vehkamäki, H., Kurten, T., Berndt, T., Petäjä, T., Worsnop, D., Ceburnis, D., Kerminen, V.-M., Kulmala, M., and O'Dowd, C.: Molecular-scale evidence of aerosol particle formation via sequential addition of HIO3, Nature, 537, 532-534, doi: 10.1038/nature19314, 2016.

Spietz, P., Gómez Martín, J. C., and Burrows, J. P.: Spectroscopic studies of the I2/O3 photochemistry: Part 2. Improved
545   spectra of iodine oxides and analysis of the IO absorption spectrum, J. Photochem. Photobiol., A, 176, 50-67, doi: 10.1016/j.jphotochem.2005.08.023, 2005.

Stone, D., Whalley, L. K., and Heard, D. E.: Tropospheric OH and HO2 radicals: field measurements and model comparisons, Chem. Soc. Rev., 41, 6348-6404, doi: 10.1039/c2cs35140d, 2012.

Stratmann, R. E., Scuseria, G. E., and Frisch, M. J.: An efficient implementation of time-dependent density-functional theory
550   for the calculation of excitation energies of large molecules, J. Chem. Phys., 109, 8218-8224, doi: 10.1063/1.477483, 1998.

Vandaele, A. C., Hermans, C., Simon, P. C., Carleer, M., Colin, R., Fally, S., Mérienne, M. F., Jenouvrier, A., and Coquart, B.: Measurements of the NO₂ absorption cross-section from 42 000 cm^{-1} to 10 000 cm^{-1} (238–1000 nm) at 220 K and 294 K, J. Quant. Spectrosc. Radiat. Transfer, 59, 171-184, doi: 10.1016/S0022-4073(97)00168-4, 1998.

555   Wei, N., Hu, C., Zhou, S., Ma, Q., Mikuška, P., Večeřa, Z., Gai, Y., Lin, X., Gu, X., Zhao, W., Fang, B., Zhang, W., Chen, J., Liu, F., Shan, X., and Sheng, L.: VUV photoionization aerosol mass spectrometric study on the iodine oxide particles formed from O3-initiated photooxidation of diiodomethane (CH2I2), RSC Adv., 7, 56779-56787, doi: 10.1039/c7ra11413c, 2017.